

ABSTRACT

Title of dissertation: WIDE FIELD OF VIEW
SPECTROSCOPY USING
FABRY-PEROT INTERFEROMETERS

Jonathan Nikoleyczik
Master of Science, 2016

Dissertation directed by: Professor Sylvain Veilleux
Department of Astronomy

We present a high resolution spectrometer consisting of dual solid Fabry-Perot Interferometers (FPIs). This work is intended to be an all inclusive documentation of the instrument including discussion of the design of this instrument, the methods used in data reduction, and the analysis of these data. Each FPI is made of a single piece of L-BBH2 glass which has a high index of refraction $n \sim 2.07$ with a thickness on the order of $100 \mu\text{m}$. Each is then coated with partially reflective mirrors to create a resonant cavity and thus achieve a spectral resolution of $R \sim 30,000$. Running the FPIs in tandem reduces the overlapping orders and allows for a much wider free spectral range and higher contrast. We will also discuss the properties of the FPIs which we have measured. This includes the tuning of the FPIs which is achieved by adjusting the temperature and thus changing the FPI gap and the refractive index of the material. The spectrometer then moves spatially in order to get spectral information at every point in the field of view. We select spectral lines for further analysis and create maps of the line depths across the field. Using

this technique we are able to measure the fluorescence of chlorophyll in plants and attempt to observe zodiacal light. In the chlorophyll analysis we are able to detect chlorophyll fluorescence using the line depth in a plant using the sky as a reference solar spectrum. This instrument has possible applications in either a cubesat or aerial observations to measure bulk plant activity over large areas.

WIDE FIELD OF VIEW SPECTROSCOPY
USING FABRY-PEROT INTERFEROMETERS

by

Jonathan Nikoleyczik

Dissertation submitted to the Faculty of the Graduate School of the
University of Maryland, College Park in partial fulfillment
of the requirements for the degree of
Master of Science
2016

Advisory Committee:
Professor Sylvain Veilleux, Chair/Advisor
Dr. Alexander Kutyrev, Co-Advisor
Professor Stuart Vogel

© Copyright by
Jonathan Nikoleyczik
2016

Table of Contents

List of Figures	iv
1 Introduction	1
1.1 Fabry-Perot Interferometer Background	2
1.1.1 Dual Fabry-Perot Interferometers	5
1.1.2 Applications of FPIs	7
1.2 Chlorophyll Fluorescence Background	7
2 Instrument Layout and Design	10
2.1 Instrument Layout	10
2.1.1 Dual Etalon Setup	11
2.1.2 Interface and Control	12
2.2 Piezoelectric Controlled FPIs	14
2.3 Cameras	14
2.4 Design and Fabrication	15
2.4.1 Filter Wheel	17
2.4.2 Vacuum Chamber Design	18
2.4.3 Thermal Control	20
2.4.4 Thermal Modeling	22
3 Observations	24
3.1 Spatial Scanning Observations	24
3.2 Spectral Scanning Observations	25
4 Data Reduction	27
4.1 Dark Subtraction and Flat Fielding	27
4.2 Image Registration	29
4.3 Panorama Creation	31
4.4 Optical Center Determination	33
5 Etalon Properties	36
5.1 Thermal Expansion Coefficient	37
5.2 Tuning	38

6	Analysis	41
6.1	Spectral Analysis	41
6.2	Line Depth Maps	43
6.3	Line Depth Maps Second Method	45
7	Results	48
7.1	Chlorophyll Florescence	48
7.2	Astronomical Observations	50
7.3	Zodiacal Light	52
8	Conclusion	56
8.1	Future Instrument Assembly	57
8.2	Future Observations	58
	Bibliography	59

List of Figures

1.1	Fabry-Perot theoretical transmission diagram and plot	4
1.2	Laser though an etalon	5
1.3	Dual Fabry-Perot transmission	5
1.4	Chlorophyll fluorescence spectrum	9
2.1	Instrument schematic diagram	11
2.2	LabView front panel	13
2.3	SolidWorks instrument render	16
2.4	Picture of the instrument	17
2.5	Drawings of vacuum chamber	19
2.6	Thermal control circuit diagram	21
2.7	Thermally modeled vacuum chamber	22
4.1	Etalon, reference, and spectral images	29
4.2	Panoramic image example	32
4.3	Center finding methods	34
5.1	Absorption and reflectivity measurements	37
5.2	Deuterium emission in thermal scan	38
5.3	Etalon contrast ratio	39
6.1	Example polar transformation	42
6.2	Example continuum fit	44
6.3	Line depth map method comparison	47
7.1	Solar spectrum and chlorophyll ratio	53
7.2	Chlorophyll line depth maps	54
7.3	Astronomical spectra	54
7.4	Astrometry result	55
8.1	Updated instrument renderings	57

Chapter 1: Introduction

In this project, I set out to build and test a Fabry-Perot instrument with the end goal to make astronomical observations and measure florescence of chlorophyll. The project itself is broken down into four major components; instrument construction, data reduction, data collection, and analysis of that data. This instrument contains two Fabry-Perot interferometers which can take high resolution of diffuse sources. I then wrote a data pipeline to reduce the data and extract spectra from each region of a field of view. With the ability to create spectra at any point in the field of view, I then used the instrument to make observations of chlorophyll florescence and astronomical sources.

The ability to achieve high spectral resolution in a small volume the Fabry-Perot interferometer and large etendue (sometimes called throughput) compared compared to the grating spectrometers makes FPI is a very attractive option for measurements of the extended objects. One example of this is chlorophyll fluorescence which can be measured by looking at the depth of different lines in solar absorption features [1]. The chlorophyll signal is spread over the entire field containing a plant and thus a remote sensing application would require high spectral resolution, to resolve the narrow spectral features, as well as spatial resolution to

separate the different source components. Another application is zodiacal light, the scattered solar radiation off dust grains in the solar system interplanetary dust cloud. Zodiacal light extends all over the sky with very small variation at solar elongations ninety degrees or more, thus forming a uniform "screen". Due to its very low brightness it is very difficult to observe with slit based grating spectroscopy [2]. Since zodiacal light does not have spectral features of its own, its spectrum is essentially solar, which can be used to discriminate it from other diffuse sources by observing the solar absorption lines [3]. This approach has been successfully demonstrated before [4].

Chlorophyll fluoresces brightly from the red end of the optical (650 nm) to the near IR (850 nm). This can be observed as a filling of solar spectral lines. This means that in high resolution spectra of plants the solar spectral lines should be shallower than those same features in a pure solar spectrum [1]. This measurement can be directly related to the chlorophyll productivity of the plant. Thus by simply taking the spectrum of a plant one can recover the efficiency at which it is converting solar radiation into energy via chlorophyll. The chlorophyll measurements will allow for high altitude observations of forests and crops to measure gross plant output and possibly be able to provide global mapping of photosynthesis.

1.1 Fabry-Perot Interferometer Background

First invented in 1897 by Charles Fabry and Alfred Perot, the Fabry-Perot Interferometer (FPI) has become an integral component in precision spectroscopic

measurements [5]. The ability to have differential transmission of light of any given wavelength is an extremely powerful tool. This combined with the ability to discriminate very fine wavelength changes make this the ideal component for a high resolution spectrometer.

Another unique feature of FPIs is their ability to combine high throughput with high spectral resolution. These two factors combined make this instrument optimal for taking spectra of diffuse objects with high spectral resolution. For most optical FPIs reflectivity of 85% is easily reached, corresponding to a spectral resolution of 30,000 at optical wavelengths [6, 7].

The Fabry-Perot interferometer operates by creating interference between its two partially reflective, plane parallel mirrors. Since the reflectivity of the mirrors is high, multiple reflections occur before the light exits out the opposite side of the FPI. The transmission through the FPI is maximal when the constructive interference condition is met. The interference condition is dependent on the incident angle θ , the index of refraction n and the separation of the mirrors l . A study of this system finds that the transmission T through an ideal FPI is only related to the reflectivity R and the phase of the light δ [6].

$$\delta = \left(\frac{2\pi}{\lambda}\right) 2nl \cos \theta' \quad (1.1)$$

$$\sin \theta' = n \sin \theta \quad (1.2)$$

$$\delta = \left(\frac{2\pi}{\lambda}\right) 2l\sqrt{n^2 - \sin^2 \theta} \quad (1.3)$$

$$T = \frac{(1 - R)^2}{1 + R^2 - 2R \cos \delta} \quad (1.4)$$

Where θ' is the angle of incidence before the FPI enters the cavity which contains

a material with index of refraction n . We have also assumed that the index of refraction outside the FPI to be unity. Also the transmission equation used here is for the ideal case in which there is no absorption within the FPI.

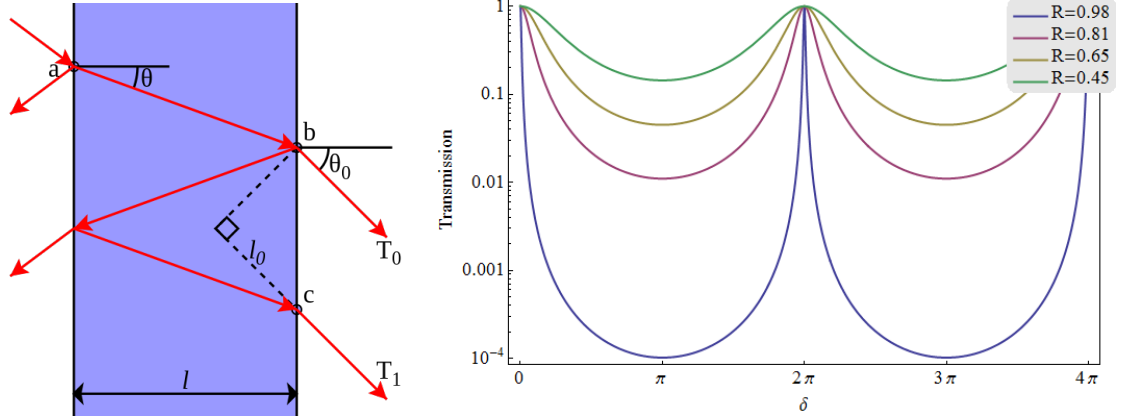


Figure 1.1: *Left:* A diagram illustrating the passage of light through a Fabry-Perot etalon; light entering from the left is observed to be amplified if the wavelength is an integer multiple of the effective path length [8]. *Right:* A plot of the transmission through an ideal FPI as a function of the phase δ for different values of R (0.98, 0.81, 0.65, and 0.45 from narrowest to widest); In our case the phase change is induced by changing the path length l and the angle θ [6].

Looking through a Fabry-Perot etalon one sees a series of rings representing the spectrum of the source one is observing, like the one shown in Figure 1.2. If any of the parameters λ , n , l , or θ change there will be a shift in the rings corresponding to that change. This allows the FPI to be used for spectroscopy by changing a parameter like the index of refraction or separation in a controlled manner [9].



Figure 1.2: An image of a diffuse laser source through a $121\ \mu\text{m}$ thick solid FPI. Here we can see that there are 3 spectral lines corresponding to the 0th, 1st, and 2nd orders of the lasing cavity.

1.1.1 Dual Fabry-Perot Interferometers

With the ability to control one etalon another can be placed in the beam. The transmission through two etalons will then simply be the product of the transmission of each individual etalon. In Figure 1.3 we can see the transmission in the dual etalon case in red has suppressed orders outside the one in consideration.

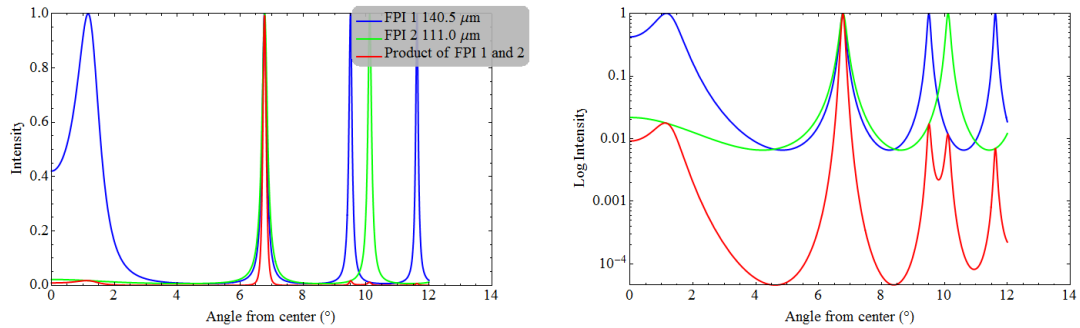


Figure 1.3: *Left:* A plot of Equation 1.4 for two etalons of different spacings (green and blue) along with the transmission of the well aligned two etalon configuration (red). *Right:* Same as the figure on the left now shown in log scale.

In order to tune a dual etalon we need the emission line peaks of two different FPIs to line up at the same angle. This is done by tuning one of the FPIs to align the orders of the other. Then the transmission through two FPIs is just the product of the transmission through each of the FPIs individually this is shown in Figure 1.3. Looking at a single emission line would show that there is significant suppression of orders outside the aligned one, while looking at a continuum would show a true spectrum of the object [10]. This is why the ability to move by a single order is so important, we need to be able to tune one of the FPIs to any setting within that order.

This does introduce some complications though. The first being that the etalons need to be very close to parallel. The optical axes of the two FPIs need to be aligned to within about 10 arcminutes [5]. To assist with this alignment we place one of the FPIs on a tip tilt mount while the other one is fixed. This gives us the freedom to move the center of the FPI and align the two rings. This is a difficult procedure, which takes a steady hand to perform correctly.

The second complication comes from the stability of the tuning. The tuning needs to be stable to within the width of the line. In our system, this means we will need a proper thermal control system.

A measure of the alignment of two FPIs is a quantity known as the contrast ratio. This describes the amount of light which passes through the FPI in regions which should be in destructive interference. The quantity C is defined as the ratio between the intensity at the point of maximal transmission the point of minimal

transmission. For the case of two FPIs with equal reflectivity (R) this is given by:

$$C \equiv \frac{I_{max}}{I_{min}} = \left(\frac{1+R}{1-R} \right)^4 \quad (1.5)$$

Note that the contrast ratio is only dependent on the reflectivity and thus should be independent of the source. We will use this quantity to check the alignment of the FPIs as a misalignment is the only factor that could contribute to a change in this value.

1.1.2 Applications of FPIs

This ability to spatially resolve spectral features has led to many different applications of Fabry-Perot Interferometers. They have been widely used in observations of solar features where the source is very diffuse and bright [5, 11–13]. Many FPIs have moved from the optical to the infrared where there is a larger difference between successive peaks. FPIs can also be used to create a tunable filter by properly adjusting the spacing to allow only a narrow spectral band [14, 15].

A more engineering driven application of FPIs is in lasers. The FPI is used to confine photons with the cavity and allow for a higher probability of stimulated emission with each reflection [9]. This same technique can be used to make a tunable laser which has applications in a variety of remote sensing fields.

1.2 Chlorophyll Fluorescence Background

The examination of the florescence of chlorophyll has been used for many years in the biological sciences to study plant efficiencies. It was discovered that

the amount of light produced from florescence is proportional to the amount of chlorophyll contained in the sample [16]. This provides a nondestructive method of measuring the efficiency of plants.

The primary method for these measurements just uses a broadband filter to measure the ratio of incident UV light to the amount of reflected florescence [17]. A problem with this method though, is that a source of UV light must be applied to the source in order to measure only the florescence component [18]. This means that this measurement cannot be made of large areas of forest to measure bulk plant activity.

We set out to measure this florescence in a different manner. Instead of applying a known source to the plant, we can instead use the sun as our source and simultaneously observe the spectrum of the sun and the plant to be studied. The florescence should have the effect of filling in the deepest part of a line of the solar spectrum. This has the effect of reducing the depth of a line and decreasing the equivalent width of that line. With our high spectral resolution, this effect is measurable [19, 20].

The effect of chlorophyll fluorescence is a very wavelength dependent effect. A simulated spectrum of the fluorescence is shown in Figure 1.4. Here we can see that the fluorescence spectrum peaks around 730 nm and drops off above 850 nm and below 650 nm. This figure includes lines corresponding to some of the filters which we will use on the instrument. Each of these filters contain deep spectral absorption lines from either the solar absorption or atmospheric absorption.

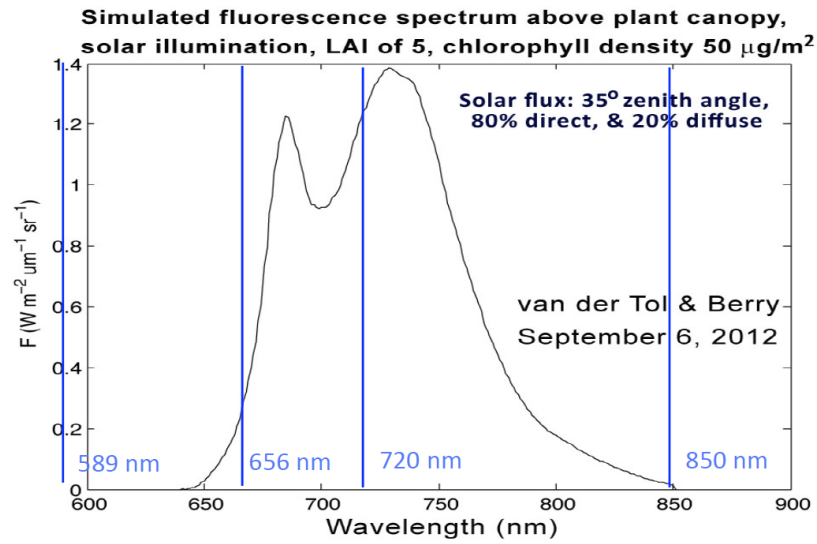


Figure 1.4: The expected chlorophyll fluorescence spectrum. Here some of the filters we will be using are noted. While this scale shows absolute flux note that we will be observing the relative change in this signal across each filter [1].

Chapter 2: Instrument Layout and Design

This chapter will include the details that went into the construction of the instrument and control software. This includes a thorough description of the layout and design principles of the instrument. Then it will cover the details of each part of the instrument. It will also describe the SolidWorks models of the instrument including the thermal modeling of those components.

2.1 Instrument Layout

The basic operating principle of this instrument is to send the incoming light into two different cameras. One camera, called the reference camera is used to record the bulk spatial intensity of the source. This light is only blocked by the filter so it contains no spectral information. The second optical path includes one or two FPIs and will then produce an interference pattern based on the spectral properties of the source [9]. This schematic layout is shown in Figure 2.1. The intensity of the light in this etalon camera will also be modulated by the overall intensity of the source. Since we have this information from the reference camera we are able to divide the etalon image by the reference and recover the original spectrum of the source.

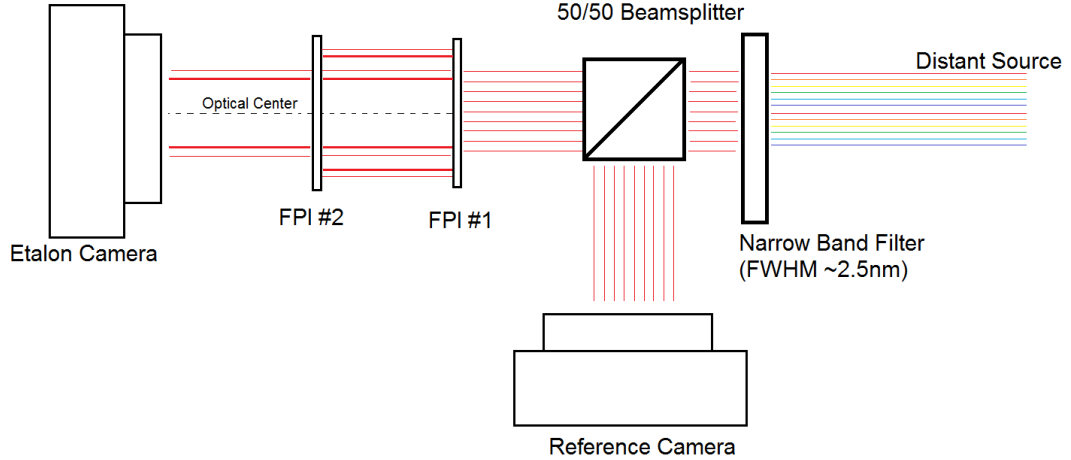


Figure 2.1: A schematic diagram showing the layout of the instrument in general. Through all the revisions and changes this layout remained constant. The only thing that was changed was the FPIs themselves from tunable controlled etalons to solid ones.

2.1.1 Dual Etalon Setup

Throughout this project we have used two different setups of the etalons themselves both of which are in a dual etalon configuration. The first case used a tunable etalon, which allowed for full control of the mirrors in 3D. These FPIs used an air gap so in order to get the same FSR required a larger separation than the later solid FPIs. This setup was largely used in the measurements of chlorophyll.

The second set of FPIs were solid with high accuracy polished plane parallel LBBH-2 glass plates and tuned by heating and thus expanding the separation. The FPI plates have been precision machined to be parallel to within ~ 5 nm. This particular glass was chosen as it has a high index of refraction of ~ 2.1 in the wavelength range of our instrument [21]. This high index of refraction has the added benefit of increasing the throughput by a factor of n^2 which is a significant factor when

observing faint sources. This increase in throughput comes from the conservation of etendue in an optical system and the etendue is given by $n^2 dS \cos \theta d\Omega$.

Another useful property of this glass is its high coefficient of thermal expansion of $C_{exp} \sim 1 \times 10^{-5} \text{ } ^\circ\text{C}^{-1}$. We use this property of the glass in order to change the separation of the mirrors. We can, using equation 1.3 which is periodic every 2π multiples of δ , easily calculate the temperature change required to shift the maximal interference by one full order [9].

$$n_0 = \frac{2\mu l \cos \theta}{\lambda} \quad n_0 + 1 = \frac{2\mu l_2 \cos \theta}{\lambda} \quad (2.1)$$

$$l_2 = l(1 + C_{exp} \Delta T) \quad (2.2)$$

$$\Delta T = \frac{\lambda}{2\mu l \cos \theta C_{exp}} \quad (2.3)$$

For our instrument $\lambda = 0.656 \mu\text{m}$ and $l = 121 \mu\text{m}$ we find that the heating required is $\Delta T \approx 55$ Kelvin. We will need to heat the FPI by this amount to properly tune the instrument, thus we require both stability and accuracy in our thermal control of the system.

2.1.2 Interface and Control

The entire instrument can be interfaced and controlled using a LabView program. This program has controls for both cameras, the etalon parameters, the filter wheel, and the telescope mount. This interfaces all of the components and records the status and monitors for any incorrect behavior.

The primary routine of the software is the spatial scan method the observations of which will be discussed in Section 3.1. The first step of the routine is to take a

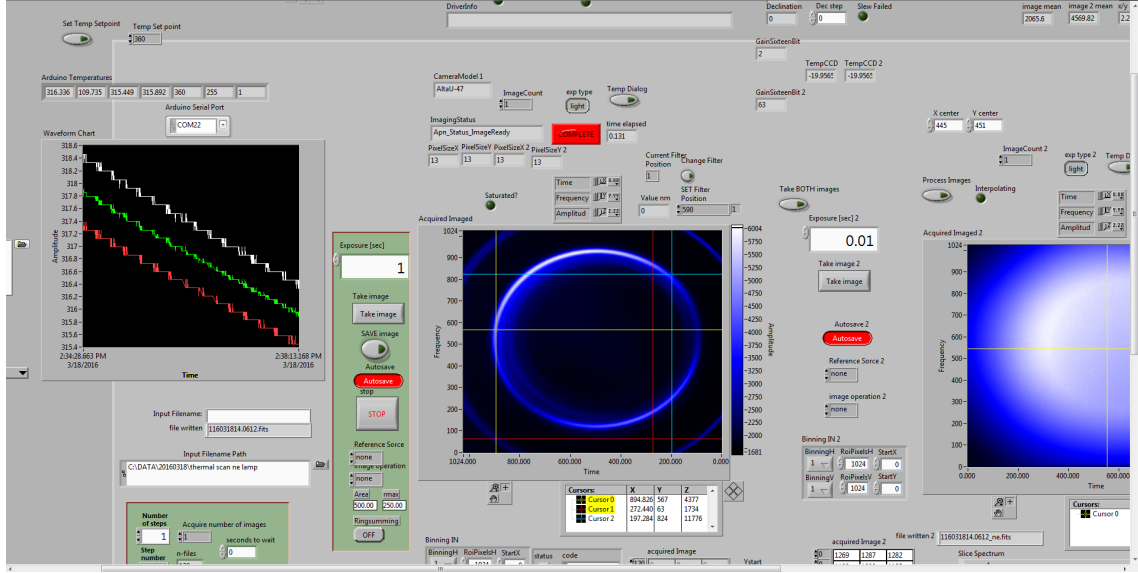


Figure 2.2: The labview control panel for the instrument. The left plot shows the temperature of the single etalon over time, the middle image is from the etalon camera and the right image is from the reference camera.

dark of the exposure time which the user has specified. If a dark of this integration time has already been taken that day then none are taken. The routine then sets the filter wheel to the requested wavelength. It then takes images in both the etalon and reference cameras, again with the integration time specified by the user. The program then saves those two images to a .fits file. This file also contains, in the header, the information about the filter, integration time, and etalon settings. The routine then moves the telescope by a specified amount and repeats the procedure until the specified number of images are taken.

The LabView program can also perform some preliminary analysis on the data. For example, it can find the optical center of the rings, which can be helpful while aligning two etalons. It can then use that center to take a rough spectrum of the data. Again, this is only used for reference to see whether faint lines exist or if

longer exposures are required.

2.2 Piezoelectric Controlled FPIs

The first iteration of this instrument used dual piezoelectric controlled FPIs. These used a Queensgate Instruments Ltd. CS100/ET servo-stabilized Fabry-Perot system, which allowed for full control of the mirrors in 3D [22]. This gave the freedom to change the parallelism and the separation; both of which could be changed over a range of about 0.1 mm in steps of 0.49 nm [23]. The properties of these FPIs were very similar to the solid ones we later fabricated. The major difference being that these have an air gap between the mirrors this means that they do not receive the throughput or FSR benefits which come from a higher index of refraction.

These were very stable and showed very little variation in tuning over a full day of observation. The only changes came from changes in the index of refraction of the air gap corresponding to temperature or pressure changes. This setup was used for the chlorophyll fluorescence measurements as they allowed us to quickly switch between tunings and thus filters.

2.3 Cameras

The cameras we used in this instrument are the Apogee ALTA model F47. These have a relatively high quantum efficiency over the wavelength range we are observing. A collection of properties of the cameras and lenses is included in Table 2.1.

Table 2.1: Properties of the cameras and lenses

Camera	
Sensor	CCD47-10 (E2V)
Sensor Dimensions	1024 x 1024
Pixel Size	13 x 13 μm
Bit Resolution	16 bit
Lenses	
Name	Nikkor AF Micro
Focal Length	60 mm
F#	32 to 2.8
Pixel Scale (Measured)	45.4 arcsec/pixel

We have found that the two cameras used in the system are very similar to each other with the only major difference being in the dark images of the two cameras. As we will discuss in more detail in section 7.2, there is a significant dark current and hot pixels in these cameras. Their sensors are an old design which is prone to column transfer artifacts and hot pixels. This became an issue when we attempted to observe faint stars. The hot pixels dominated the signal and appeared brighter than the stars. We intend to purchase new cameras which will have much better read noise and dark current.

2.4 Design and Fabrication

In order to machine parts and check clearances it is important to have an accurate 3D model of the instrument. We used Solidworks to create a working 3D model of the instrument; the current iteration of which is shown in Figure 2.3.

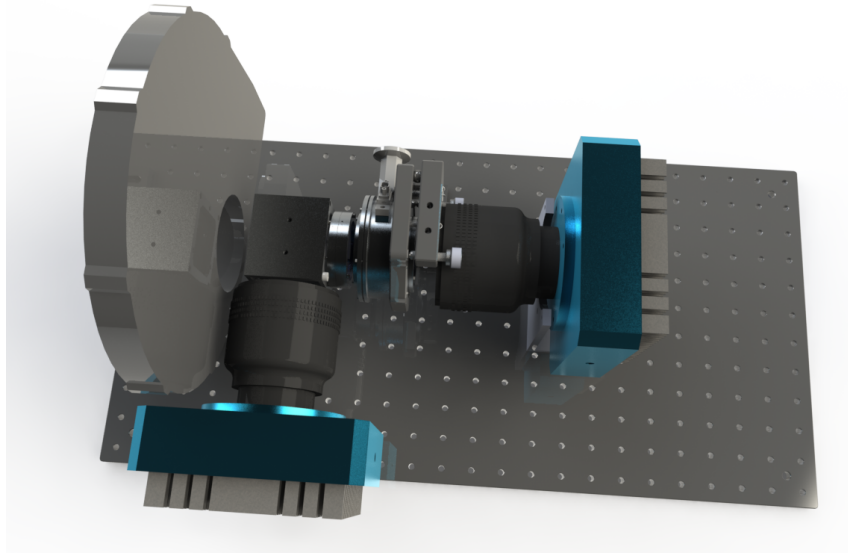


Figure 2.3: A rendering of the instrument showing the layout of the cameras and two etalons, one inside the vacuum chamber and the other attached directly to the beam splitter.

From there, We were able to design the components we required. These components include holders for the etalons, a vacuum chamber, a beam splitter mount, and light baffles.

We have designed a mount for the solid Fabry-Perot interferometer. This mount then needed to be thermally isolated from the rest of the system, so I designed a vacuum chamber to mount the holder in. The chamber also needed feedthroughs for electrical connections and a vacuum pump which we purchased. After completing the design and thermal modeling of the vacuum chamber and etalon holder we had them machined at the GSFC machine shop. We then designed a thermal control system which regulates the temperature of the etalon while in the vacuum chamber. We tested this system in air and it is able to keep the temperature within 0.1 Kelvin of the set-point temperature.

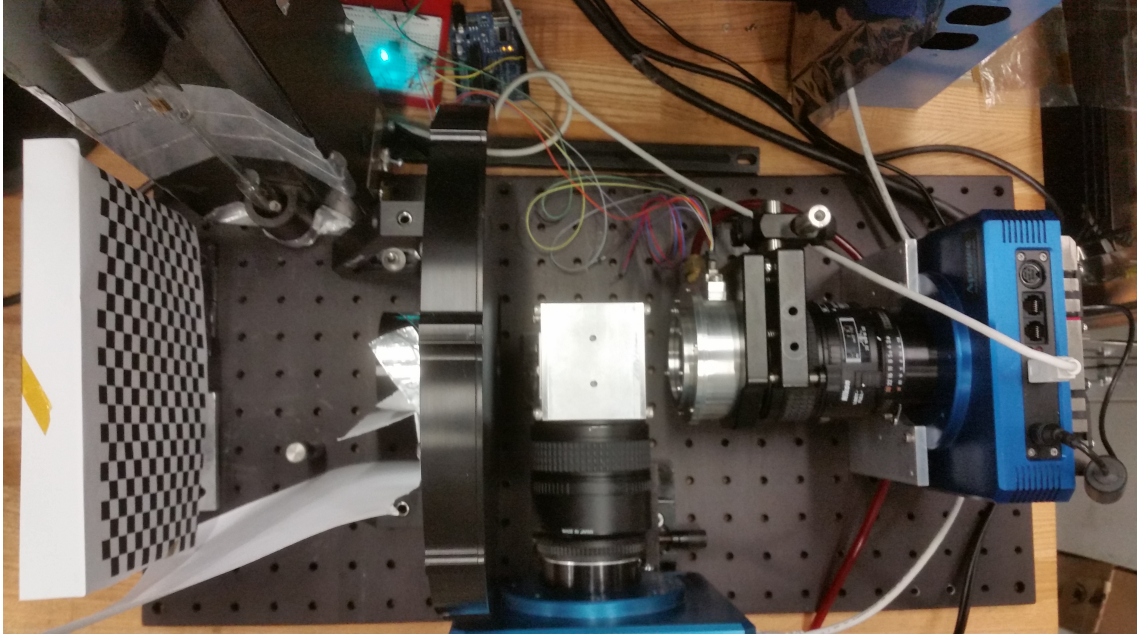


Figure 2.4: An image of the instrument in its current configuration. Here we have one etalon inside the vacuum chamber in front of the blue camera on the right. The beam splitter is in the center of the image. On the left hand side I am observing a reference checkerboard pattern to check the alignment of the two images.

2.4.1 Filter Wheel

The first component in the optical path is the filter wheel. It blocks the orders outside the region of interest using one of 9 different narrow band filters. These limit the spectral band of the incoming light to reduce the overlap of orders in the FPI. With a single FPI there is still overlap of orders but adding the order blocking filter significantly reduces the impact of extraneous orders. The central wavelengths for the filters and their corresponding FWHM are included in Table [2.2](#).

We chose these wavelengths as our sources of interest have deep absorption features in all of these filters. The significant features include the sodium doublet at

Table 2.2: The central wavelength and FWHM for the filters on our instrument ordered by their position in the filter wheel.

Filter Position	1	2	3	4	5	6	7	8	9
λ_{center} (nm)	589.7	720.9	740.0	740.0	720.9	641.3	751.3	853.6	656.3
FWHM (nm)	3	3.5	1.5	3	2	3	3.7	4.3	3

590 nm, $H\alpha$ at 656 nm, and terrestrial atmospheric H_2O absorption at 720 nm [24, 25]. The reason to observe the deepest features for our application is that we will be looking for the difference in absorption features in different spatial locations. This difference will be strongest when the absorption features themselves are deep.

2.4.2 Vacuum Chamber Design

In order to keep the temperature stable and allow the etalon to heat the required 55 K we decided to put the etalon inside of a vacuum chamber. This chamber needed to have feed-throughs for electrical components as well as be able to fit on a tip tilt mount. The feed-throughs would be for the heaters and the temperature probes while the tip tilt mount would allow for the alignment of the two etalons with respect to each other. After many revisions we came up with a 3 inch in diameter chamber with a door and two holes to mount windows to.

The next issue was insulating the etalon from the chamber, as there will be a significant temperature gradient between the two. I decided to use garolite, also known as G-10, to make feet that connect the etalon to the chamber. This has a very low thermal conductivity, while being structurally very strong and stiff. The

other way to reduce thermal conductivity was to make these feet as thin as possible while maintaining structural stability.

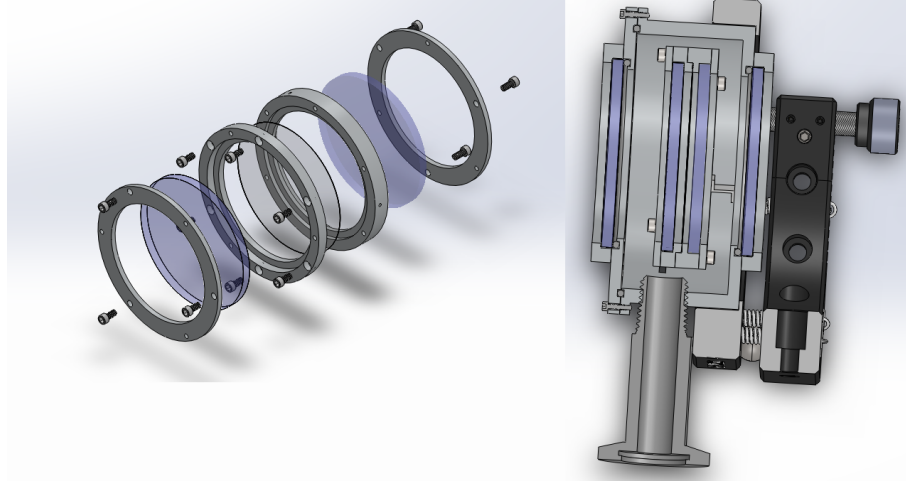


Figure 2.5: *Left:* A SolidWorks exploded diagram of the etalon ring holder. *Right:* A cross section of the vacuum chamber showing the ring holder in the center and the tip tilt mount on the right.

We then needed a mount which would keep the etalon in contact with the heaters as well as providing a way to clamp it in place. To accomplish this we designed a series of aluminum rings shown in Figure 2.5. These rings clamp the etalon and have slots on the front and the back to hold two sapphire windows. The clamping of the etalon was chosen to minimize the amount of stress on the etalon through the entire range of the heating [26].

The reason to minimize the stress on the etalons is that they are very fragile. At only about 100 microns thick there is very little material to provide rigidity. Imperfections from the manufacturing process occur at the edges so cracks can easily spread across the etalon. Two of our etalons have cracked, one during the coating process by the manufacturer and the other while testing before the construction of

the mounting ring.

The primary reason to use sapphire in this etalon holder is the fact that it at least is 90% transmissive over our entire wavelength range while at longer wavelengths it quickly becomes absorptive. This means that it will be a strong emitter of radiation with temperatures below 140°C. This property means that there will be a strong radiative coupling between the sapphire windows and the etalon thus we do not need to entirely rely upon conduction to transport the heat to the center of the etalon. The windows also have the added benefit of protecting the etalons.

2.4.3 Thermal Control

In order to heat the etalon and keep the temperature stable we needed to design a thermal control system. To do this we used an Arduino programmable microcontroller to read temperatures and turn on and off the heaters. The Arduino code is relatively straightforward and uses a Proportional Integral Derivative (PID) control system to determine when to turn the heaters on in order to keep the temperature as close to some set point as possible [27]. The Arduino then sends the information about the temperature and heater status to the LabView software to be recorded.

The heaters are powered by an external power supply which allows us to vary the input power, which although not necessary, is very helpful in changing the heating rate. The heater is turned on via an optoisolator with the switch being controlled by the Arduino. This component limits the amount of current leak from

the power supply back into the Arduino.

The heater is made from wrappings of a very thin gauge Manganin wire. This wire has a very high resistance per length while maintaining a low fuse current and high thermal conductivity. We wrapped the etalon holder in 17 windings of this wire which gave a resistance of 181 Ohms. Powering the heater with a benchtop power supply of 23 V would then provide 2.92 W of power to heat the etalon. This is the typical operating voltage at the upper limit of our temperature range.

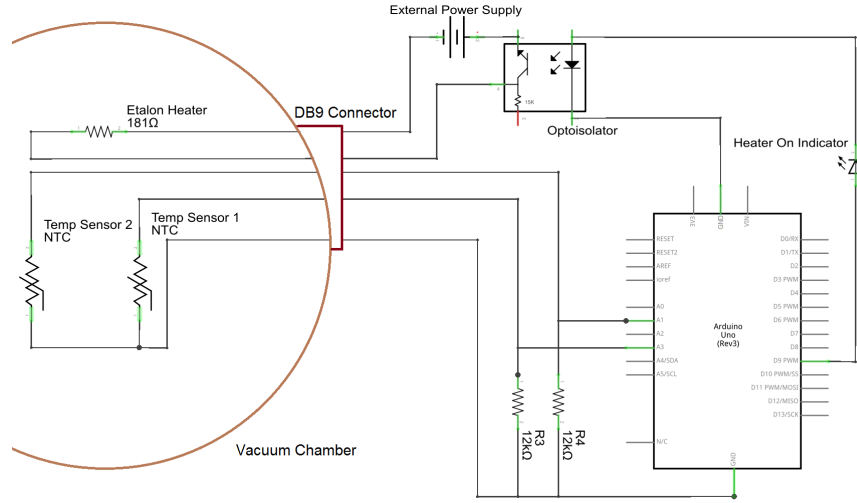


Figure 2.6: A circuit diagram of the etalon heater control system. The left side of the system is contained within the vacuum chamber and includes two thermometers on the ring holder. The Arduino is shown on the right side along with the control switch.

The thermometers we use are NTC thermistors which have a known resistance versus temperature curve. We can then use the Arduino to measure the resistance of the thermistor and use this relationship to determine the temperature. In the future these thermistors will be mounted to the etalon holder using stycast to ensure thermal contact but currently they are simply taped to the etalon holder.

2.4.4 Thermal Modeling

Since we have a very accurate Solidworks model of all of these components it was very easy to simulate the thermal leaks and heating rates. We modeled the heaters, the loss through all of the materials involved, radiative losses and convection. We found that the losses through the G-10 feet was insignificant at 0.2W of heat loss while the etalon was being heated with 3.5 W of power. We also discovered that the radiative coupling between the etalon and the sapphire windows has a significant impact on the temperature across the etalon.

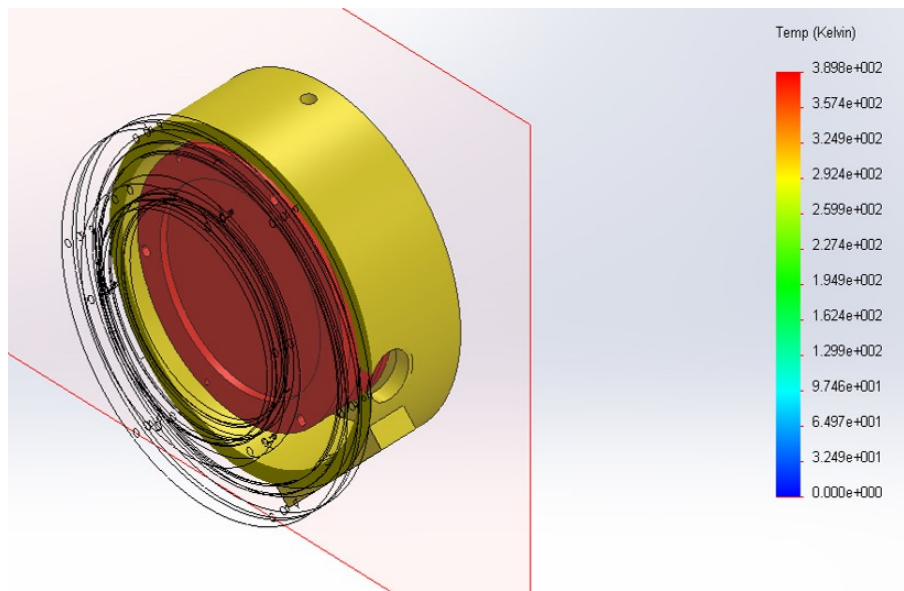


Figure 2.7: A cross sectional view of the thermal modeled vacuum chamber system. This model includes both radiative and convective losses. Here we can see that there is still a significant difference in temperature from the etalon holder to the walls of the chamber.

While testing the heaters we noticed that we got similar heating rates regardless of whether or not the vacuum pump was actually on. We then attempted to

model this assuming a convective coupling between the walls of the chamber at room temperature and the etalon heated by 3.5 W and indeed noticed a very small change in the steady state temperature. This is likely because the chamber is closed so the heat must be convective only by its own bulk flow rather than forced convection. Because of this we are currently able to run the chamber at atmospheric pressure though we can easily add a vacuum pump at any time.

Chapter 3: Observations

Using our instrument we are able to demonstrate two types of measurement techniques; one which scans a field of view spatially with constant FPI tuning while the other makes a constant pointing and changes FPI settings scan spectrally. These two different methods are used to create a data cube in which the spectral dimension of the cube either corresponds to the location of the optical center or to the spacing of the FPIs. Both methods have their strengths and complexities depending on the available data from the set of observations.

3.1 Spatial Scanning Observations

The spatial scanning method uses a constant etalon tuning while moving spatially. This allows us to target one wavelength range with high resolution. Since we would like to recover the spectrum at every point in the field of view we can scan the instrument spatially and then reconstruct the spectrum using the techniques to be discussed in [Section 6](#).

This method has the significant advantage of not requiring the FPI settings to be changed. The FPIs are set to one spacing for each filter, which can be determined in advance. Once the FPIs are each set the observations can be made in quick

succession so that the source will stay constant over the course of the scan. The LabView software is able to control the telescope mount which then takes steps in right ascension or declination. The instrument can also be moved by hand so long as it does not move more than one image length between images. This allows the data reduction software to find the offset between images without getting lost.

The observations taken using this method were taken at Goddard Space Flight Center. This area allows for simultaneous observations of the sky and a large tree. This tree is the primary focus of the observations of chlorophyll florescence. It covers a large area and has a sharp contrast against the sky so it allows for easy discrimination between the two regions.

This method was also used to make astronomical observations. In this case there are two options to scan. One is to use the mount of the instrument to scan in set increments of RA or Dec with tracking on. The other option is to turn the tracking off and allow the objects to move across the sky with a constant altitude and azimuth. This second method was chosen during our astronomical observations as the motion of the sky corresponds to 52 minutes to cross the full 13 degrees of our field of view. With one minute exposures this corresponds to about 30 images to move from the center of the optical axis to the edge of the image.

3.2 Spectral Scanning Observations

The other method used to collect spectra is an FPI setting scanning method. In this method, the pointing of the instrument is kept constant and the FPIs are

tuned to different wavelengths by increasing the temperature and thus expanding the space between the plates. This method was primarily used in testing as it allowed us to take measurements on a tabletop without moving the instrument. This also assisted in the measurements of the tuning of the FPIs as the tuning could be adjusted as the temperature could be adjusted and the source could be monitored for any changes in brightness.

This method was also used extensively while testing the properties of the FPIs. This is because in that case the pointing of the instrument is not important. Scanning through orders is commonly used in other Fabry-Perot instruments as it does not require the software alignment which we will show in [Section 4.2](#).

Chapter 4: Data Reduction

The most significant challenges involved in this project were in the analysis of the data. The analysis consists of four major components, the flat fielding, image registration, optical center locating, and spectrum creation. The process of data reduction varies depending on the method used to collect the data so this will discuss a general analysis procedure. At the end of the analysis we will have extracted a spectrum from our data cube within some chosen region of a field of view.

4.1 Dark Subtraction and Flat Fielding

The flat fielding method used follows a standard astronomical procedure [14, 28, 29]. This process is the same for both the FPI camera and the reference camera using their respective dark and flat images. Before data collection a series of both dark images and flat fields are taken. The darks are taken with the shutter of the camera closed. The images have the same exposure time as the planned exposure times of the scientific images.

The flat field images are then taken with a halogen lamp, which has a flat spectrum over the region of all of our filters. To obtain a flat image we used a thick diffuser in front of the aperture. The source itself is fairly diffuse but adding the

diffuser allow for a much wider region which is flat.

Some of the very early data sets, before we realized their importance in this process, lack flat field images. In these cases we can attempt to create a flat field image using the spectral data. To do this, we essentially require that the spectral data be flat over the entire field of view of the image. We take the spectrum along a series of rays from the optical center. We then fit the maxima of the spectrum with a first or second order polynomial. This polynomial should reflect the required flat along that ray.

Once we have collected or created the flat and the dark images we can combine them to create master flat and dark images. We can then combine the darks and flat images to create master images which will be used on all of the images in the cube. To create a master dark image we take the median of all the dark images with the same exposure time, this will eliminate any cosmic rays or other spurious events from the dark images as well as reduce the variation due to readout noise [28]. We subtract the dark image from the camera images as well as the flat field images.

Once the darks have been subtracted from all of the flat images we can create a master flat image by taking the mean of all of the flat images. This reduces the impact of any changes in the source over the course of the flat field collection. With the master flat created for both the FPI and reference cameras we can then divide both true images by the flat field images. This removes a majority of the vignetting which has been common in our images. This also introduces some noise on the outer edges of the image where there is almost no light, even in the flat image. We account for this noise in the spectral analysis by limiting the field of view to the

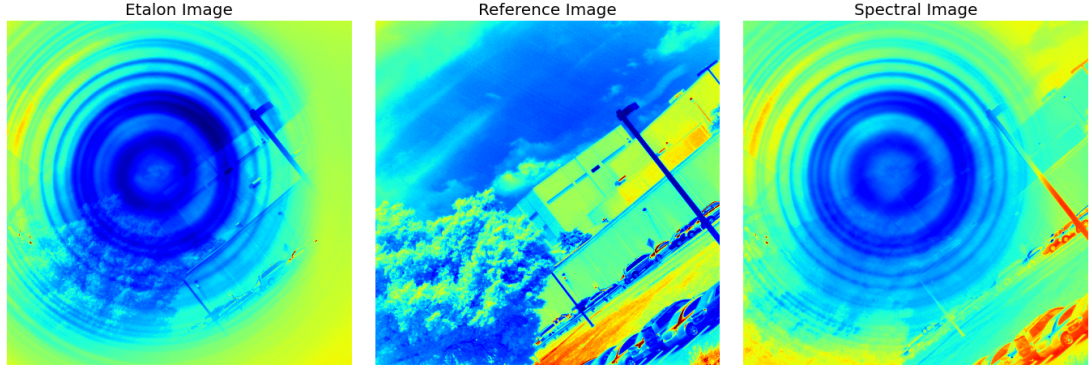


Figure 4.1: An example of the image alignment and division process. The left and center images are the FPI and reference images, respectively, after dark subtraction and flat fielding. The right image is the spectral image made from aligning the FPI and reference images then dividing them.

region where the noise is not significant.

4.2 Image Registration

The biggest challenge of this project was in recovering the relationship between two images which have slightly different pointing. Looking at our setup, we can see that a slight misalignment of the reference and the FPI cameras means that the two cameras will see different parts of the same source. We use an image registration procedure to recover the matrix that can be used to transform the reference image to match the source. An image registration procedure is also required when we need to recover the transformation to combine different reference images. This required a robust procedure to find features in an image and then find points that are common to both images. Since we use the same method for finding transformation matrices in both end goals we will discuss the general procedure of matching two images

below.

The image registration procedure uses the Speeded Up Robust Features (SURF) feature detection method [30]. This looks for features in Fourier space which represent sharp and spatially distinct features in the image. The search for features involves both filters and blob detections on the Fourier transformed data [31]. Once the features are found in both images, we use a Random Sample Consensus (RANSAC) method to find the features which are visible in both images [30]. After the inliers are discovered we can use those points to find a homography matrix that would allow one image to be transformed into the other [32].

Once the optimal transformation matrix is discovered we make some checks to be sure that the transformation matrix is reasonable. The biggest of these checks is to make sure the matrix is close to an affine transformation. The homography transformation is more general than an affine transformation but in all of our images the focus of the camera and the nonplanar features of the image should not change. This means that any transformation matrix should be almost entirely shift and rotation transforms and thus should be close to affine transformation.

The SURF image transformation technique performs very well for data in which sharp edges can be found, like those in the chlorophyll analysis. This method fails though when supplied with the astronomical images discussed in Section 7.2. This could be fixed with a proper star tracking routine but since the observations thus far have focused on more diffuse sources the astronomical observations will have a slightly different analysis.

With the routine to find a matrix transformation between two images we can

now input the FPI and reference images to find a transformation between these two cameras. After transforming the reference image to match the FPI image we can divide the FPI image by the reference image. This will leave only the spectral information encoded into the rings of the FPI image. An example of this process is shown in Figure 4.1, note here that there is a significant difference outside of the region which the FPI covers. In the final analysis this region will be masked out to leave only the region which contains spectral features.

4.3 Panorama Creation

Using the methods discussed in the previous section we can automatically create a panoramic image from an arbitrary set of reference images. With the routines to find the transformation between two images, this process is straight forward. The transformation is found between every image with respect to the previous image. Transformations are then applied in series and then images are the averaged together [31].

The procedure is robust but can become lost when there is a big step taken in separation or if there are few reference points in the images. This is accounted for in two ways. First, the collection procedure uses a stepping scheme so all the steps should be of the same size so if no transformation is found, the previous transformation will be used instead. The second way of accounting for offsets is that if the procedure gets lost it looks for possible transformations from the lost image to all of the other images. This can be very helpful when there are few

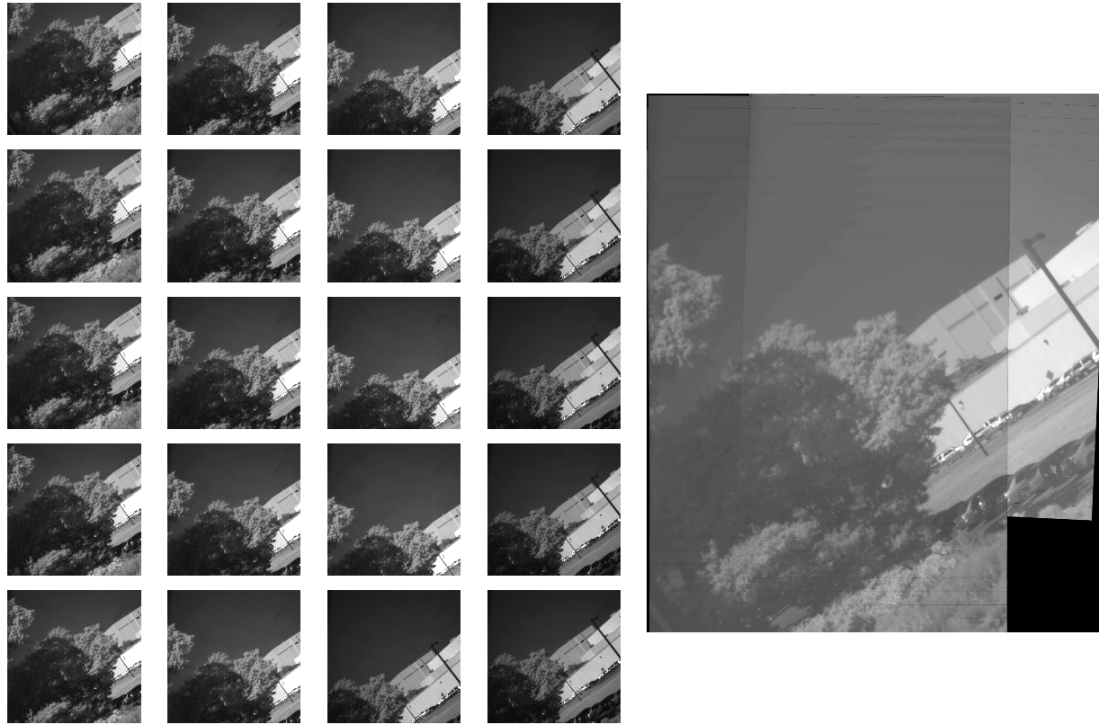


Figure 4.2: An example of the panorama creation routine. *Left:* The constituent reference images. *Right:* The composite panorama image created from the reference images on the left.

reference points in an image [33].

With all of the transformations the last step before applying them is to find the box that bounds the panorama. This is done by computing the transformations of all of the corners of all of the images and the largest corner values become the new corners of the final panoramic image. A new image is created with that size and then each image is inserted with its respective transformation applied.

4.4 Optical Center Determination

The next step in the image processing routine is to find the optical center of the spectral image. Determining the optical center of the Fabry-Perot is very important as it will be used to determine the spectra within the image, as this is measured radially from the optical center. Any offset from the true center will increase the width of a line when we average it about the optical center.

The first method we use is a rough indicator for the location of the center, which utilizes the gradient in the horizontal and vertical directions. There should be one point which minimizes the radial gradient and this point should be the center. To find this point we minimize the linear system:

$$\begin{pmatrix} \partial_y I^2 & -\partial_x I \partial_y I \\ -\partial_x I \partial_y I & \partial_x I^2 \end{pmatrix} \begin{pmatrix} c_x \\ c_y \end{pmatrix} = \begin{pmatrix} \partial_y I^2 X - \partial_x I \partial_y I Y \\ -\partial_x I \partial_y I X + \partial_x I^2 Y \end{pmatrix} \quad (4.1)$$

Here $\partial_x I$ and $\partial_y I$ are the x and y gradients of the image, respectively. We can quickly compute this derivative in either direction by using the gaussian derivative image kernel and then convolving. This is a very efficient process and gives a good approximation to the derivative at each point. We rescale the right hand side of Equation 4.1 by X and Y which are the column and row number of each pixel. Now this linear system is very easily solved using a least squares solver to find the pixel location of the center $\begin{pmatrix} c_x \\ c_y \end{pmatrix}$. This method can find the optical center for images which contain very deep lines with sharp contrast but for diffuse images a better method for finding the center is required.

The second method finds emission or absorption line along rays from an esti-

mated center, we then find the center of these points using different methods. The routine computes the estimated center using the previous gradient method which, even in the worst cases will find the center point to be near the true center. It then takes the data of the image along rays coming from the estimated center. It then find the deepest or brightest lines along each of those rays, using a method discussed in the next section. It then uses the maxima, minima, or both to determine the points which should be located radially within the image.

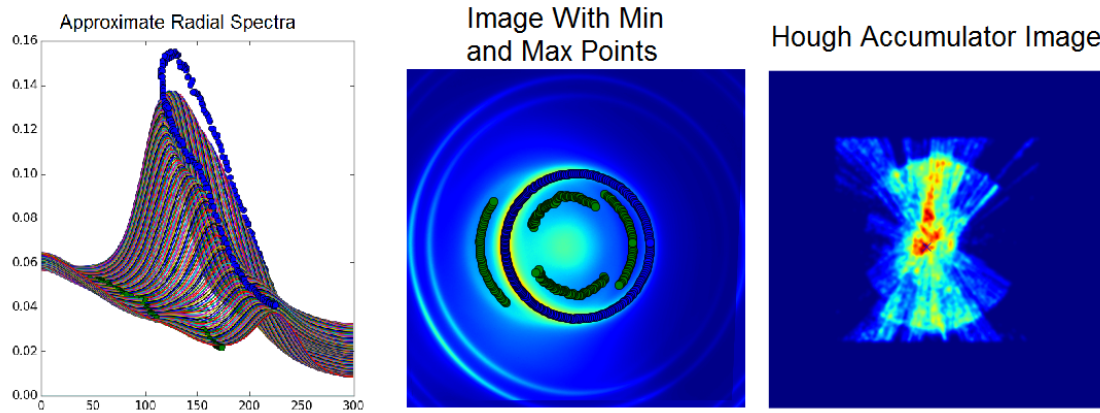


Figure 4.3: An example of the Hough center finding method. *Left:* The estimated spectra along test rays from the given approximate center of the provided image, with the local minima and maxima plotted in green and blue. *Middle:* The provided image, here a deuterium emission image, with the local minima and maxima again in green and blue. *Right:* The output of the Hough circle method, with the accumulation of all of the test annuli, redder corresponds to a stronger central signal. An x is placed on the located center which is at the maximum of the accumulation image.

From a collection of points which lie on the circles we can use two different methods to find the center. The first is to again solve a linear system but this method assumes that there is only one radius of data points. When this is the case, this method is the most robust as it exactly solves for the best fit circle. A check is

performed to see if there is indeed only one radius and if not the program moves on to the next method.

The second method is based off of the Hough circle transformation [30]. The objective of this method is to transform each point into the parameters which describe its location. For each point we increment an image with a series of concentric circles at varying radii. This is repeated for each found point. This creates an accumulation image which contains high values in regions where there is significant overlap from radii of different points. Even with some scatter in the location of the found points from a perfect circle this method is able to recover the center. This gives a robust way to locate a single center of concentric rings of different radii. The issue with this method though is that it is very time consuming. For 256 points this takes on the order of 5 minutes to complete. The trade off though is that it is able to find the optical center of nearly any image. It is robust against low contrast, multiple centers, and diffuse features.

Chapter 5: Etalon Properties

With the methods discussed in the previous chapters, we were able to make multiple measurements of the characteristics of the FPIs. These include the thermal expansion coefficient, thickness, eccentricity, and the proper tuning of a two FPI setup. The primary purpose of these measurements is to be able to determine the tuning that would be required at any wavelength. We used Geissler tubes as bright emission sources to determine most of these properties of the material. We mainly used Hydrogen, Deuterium, and Neon for these tests as they all have bright lines in at least one of our filters [\[34\]](#).

Many of the properties of the etalons we have received from the manufacturer. They have provided us with data on the transmission of the etalons as a function of wavelength which, assuming no absorption, we can easily convert to the reflectivity given that $R + T = 1$. This is plotted on the left side of [Figure 5.1](#). As proof that the no absorption assumption is valid we also include in that figure a plot of the transmission for an uncoated piece of 10 mm thick L-BBH2 glass. Note that the transmission for our glass should be closer to 1 as it is 100 times thinner than this. This still shows that there is very little intrinsic absorption of the glass.

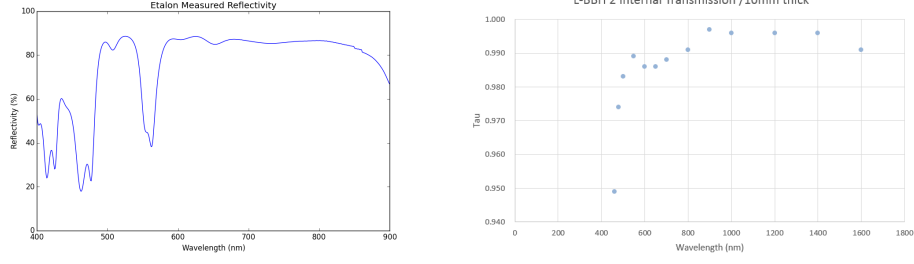


Figure 5.1: *Left:* A plot of the measured reflectivity as a function of wavelength for our etalons, assuming no absorption. *Right:* The internal transmission of a 10 mm thick piece of uncoated L-BBH2 glass provided by OHARA Inc.

5.1 Thermal Expansion Coefficient

The method for measuring the thermal expansion coefficient was to heat the material using the thermal control system and observe how the rings changed with temperature. The complication of this method, is that the material's index of refraction is also a function of temperature. To correct for this we used previous measurements of the index of refraction as a function of both wavelength and temperature [21]. We then used the methods discussed above to take the spectrum of a Hydrogen discharge tube as the FPI was heated. This changes the plate separation linearly as a function of temperature, as shown in Equation 2.3 and graphically in the left side of Figure 5.2. In the figure we see a linear relationship between the emission line location ($\cos \theta$) and the temperature. The slope of this line gives the relationship between order number and temperature.

Plotting the order number of the peak versus temperature shows a clear linear relationship, as shown in Figure 5.2. If we then fit this with a line then the slope

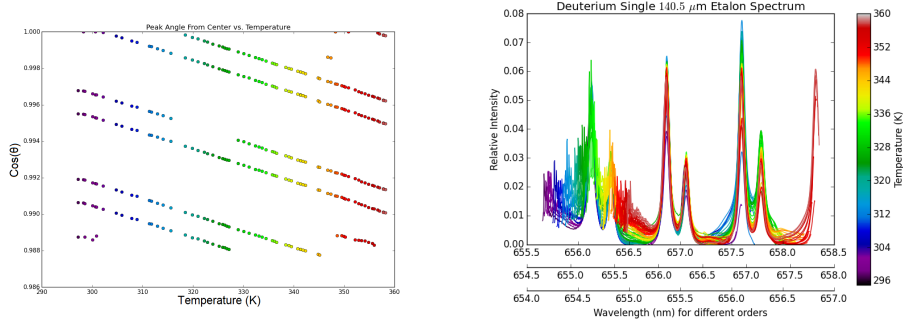


Figure 5.2: *Left:* This plot shows the location of the emission line peaks in a deuterium spectrum as a function of temperature. The vertical axis is the $\cos \theta$ measured with respect to the optical axis. *Right:* The same set of spectra of deuterium scaled to correspond to the order number (Equation 1.3) including a thermal expansion coefficient of $8.5 \times 10^{-6} \text{ }^{\circ}\text{C}^{-1}$ which shows good alignment of the peaks.

of that line should give the thermal expansion coefficient of the glass. This is done and then applied to the data shown on the right side of Figure 5.2.

We determined the thermal expansion coefficient to be $8.5 \pm 1.2 \times 10^{-6} \text{ }^{\circ}\text{C}^{-1}$. Which is consistent with the manufacturer data sheet which quotes the thermal expansion coefficient to be $8.4 \times 10^{-6} \text{ }^{\circ}\text{C}^{-1}$ at $20 \text{ }^{\circ}\text{C}$ and $1 \times 10^{-5} \text{ }^{\circ}\text{C}^{-1}$ at $100 \text{ }^{\circ}\text{C}$.

The effect of both the thermal expansion coefficient and the change in index of refraction combine to reduce the heating required to heat the FPI over one free spectral range. For an $121 \text{ } \mu\text{m}$ thick FPI the heating required is only 55 K.

5.2 Tuning

The tuning of two FPIs is crucial in being able to take proper spectra of an object. The FPIs need to be tuned to within 1 Kelvin for the spectra to have the high contrast required for our observations. When the FPIs are out of tune the orders

outside of the one in tune begin to contribute significantly to the observations of the spectrum. With proper tuning, these external orders can be suppressed below 1% thus giving a high contrast. One measure of this tuning is to observe the contrast ratio of a strong emission line, which is given by Equation 1.5 as the ratio between maximum and minimum of the transmission. This value should have a strong peak when the two FPIs are aligned [35].

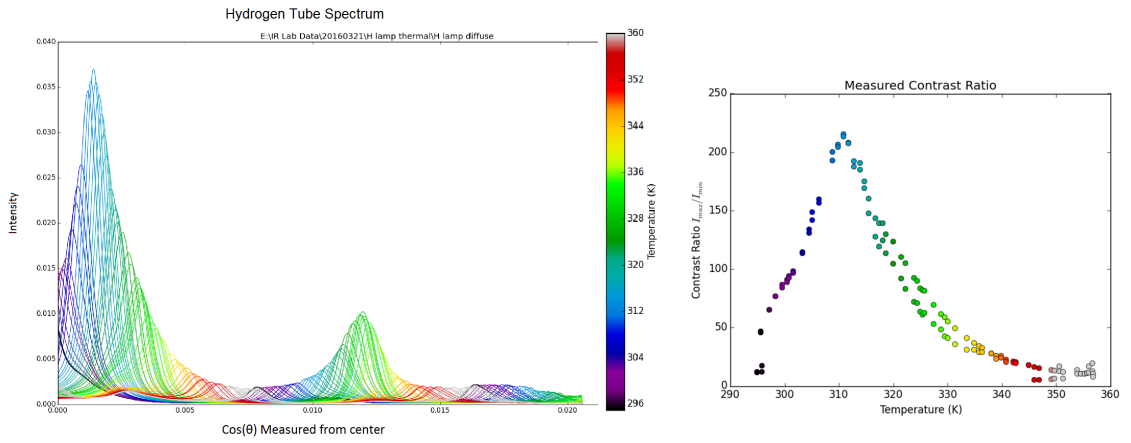


Figure 5.3: *Left:* A spectrum of hydrogen at a series of temperatures from 295 K to 355 K with two FPIs. Note that each temperature only has one peak which moves with temperature and increases in intensity at alignment. *Right:* The contrast ratio of the data shown on the left, this shows a very strong peak at 312 K.

In the right side of Figure 5.3, we can see an example of the tuning procedure. The FPIs are aligned and the temperature is changed while observing a discharge tube. This allows for a measurement of the contrast ratio of the instrument.

The contrast ratio is also a sensitive function of the alignment of the two FPIs. A slight misalignment can significantly reduce the contrast ratio by allowing more light to leak through regions of the FPI that should be receiving a minimum in

intensity. The highest contrast ratio observed for $H\alpha$ was 210. If we take the known reflectance of the FPIs and plug it into Equation 1.5 we find it has a maximum at 213 at this wavelength. This implies that we were observing an almost perfect alignment of the optical centers.

Chapter 6: Analysis

With the tools for reducing the data we will now discuss the true analysis of that data. This focuses on the methods used to construct a spectrum at an arbitrary point in the field of view and thus the construction of maps which display the line depth over the image.

We will define the depth of a line to be the fraction of the intensity within an absorption feature compared to the intensity in the fit to the continuum of the source. With this definition a deep line would have a line depth less than one while a value of unity corresponds to no line detected.

6.1 Spectral Analysis

Once we have created the images of the spectral data and found the optical center we are able to begin the analysis of the spectra in the images. The first step in the analysis is to convert the image from a radial pattern into polar coordinates around the optical center. This then means that the spectrum can be computed by taking the average along the azimuthal direction. In order to accomplish this, the routine uses a coordinate transformation mapping which takes the input coordinates and the output coordinates which maps each point to its corresponding radial and

azimuthal coordinate. This transformation distorts the spatial information but then has the intensities corresponding to any particular wavelength as a single column in this polar image. An example of this is shown in Figure 6.1.

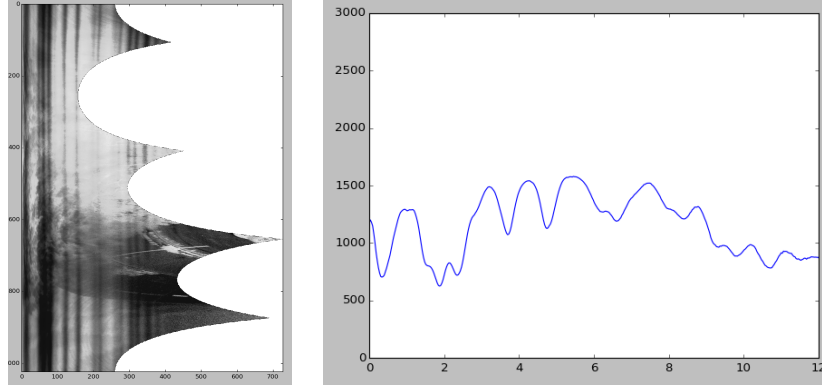


Figure 6.1: *Left:* An example of an image which has been converted to polar coordinates. The horizontal direction shows the radial component and the vertical direction shows the azimuthal direction. *Right:* The spectrum created by taking the average of each column in the image shown on the left. Note here that the x-axis is in arbitrary units which are proportional to wavelength.

To create the average spectrum over any part of the reference image we simply select that region in the reference image and then using the necessary transformations we find that region in the FPI image. We can then apply the polar transformation to the masked FPI image. To find the spectrum of that region we simply take the mean of each column which correspond to regions at equal radii. This averages over the spatial dimension of the region while extracting the average spectrum of that region. The radial coordinate is then taken from Equation 1.3.

Now that we have a method to create a spectrum from an arbitrary region of the image we can do analysis on the spectrum of any region within the image. This is shown in right right side of Figure 6.1, where each data point corresponds to the

mean intensity at some radius. Using the panorama method discussed in Section 4.3 we can reconstruct a spectrum using the transformations provided by the routine. The user can then select a region in the panorama image and recover all the sections of the FPI and reference images which make up the chosen region.

With the ability to recover any part of spectral image simply by selecting a region on the panoramic image we can easily recreate the spectrum of that region. We simply extract the spectrum of each of the individual spectral images then stitch them together in a coherent way.

6.2 Line Depth Maps

Up to this step we have created a series of spectra at different radii all corresponding to one region on the panorama image. Now we need to combine these into a single spectrum at that point on the image. To accomplish this we take the average of the points at the same radii. There is some fluctuation of the components of the spectra because of errors in the zero level of the division process. This comes from the uncertainty of the noise during the true exposure. To correct this we use a moving average across the spectrum with a window width of 5 pixels. This suppresses fluctuations from outliers while not changing the overall shape of the spectrum.

Once we have created a composite spectrum of a region we would like to determine different properties of that spectrum, namely the depth of any lines in the spectrum as well as the full width at half maximum (FWHM) of those lines.

To accomplish this, we need to first find the locations of the minima and maxima. We then estimate the level of the continuum. To do this we make the assumption that the maxima of the spectrum is the continuum. This assumption works well for regions with many lines but it struggles in regions where there is little information about the continuum. Once we make that assumption about the continuum, we simply fit a line between them and find the value of the continuum and take the ratio of the continuum to the minimum to be the fractional depth of the line.

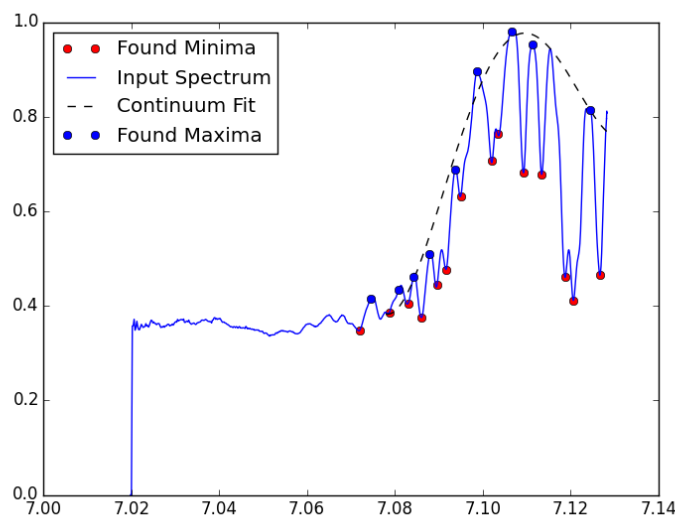


Figure 6.2: An observed spectrum in the 720 nm filter, with the 4th order polynomial fit to the continuum and the locations of the minima and corresponding locations on the continuum. The x-axis is proportional to wavelength and the y-axis is an arbitrary intensity.

To get the FWHM of a line we use the same fit to the continuum as used to find the depth. Now we just take the region between the two maxima to be the full extent of the line. Then we just find the half max then measure the width at that

point.

To create a line depth map, we sample some region of the field of view and construct its spectrum. We can then use the methods discussed above to find the line depths of all the lines in that field of view. We then color that region corresponding to the average depth of the lines within that region. This is then repeated many times over about 10 region sizes and covering about 2,000 regions. The composite image of all of these regions is then the final line depth map. An example of the results of this method is shown in Figure 7.2. In this figure, we can see that there is a strong signal among the different regions. There are also some artifacts on the edges of the maps, these correspond to regions where there is very little data about the spectrum. Since the quality of the spectrum drops away from the center these points around the edges are ignored, thus the mean line depth is one, showing no depth change.

6.3 Line Depth Maps Second Method

While testing the robustness of the previous method, we encountered some issues and decided to attempt a different method to produce the depth maps. The biggest issue was that the previous method oversampled the data. It made repeated observations of small regions of the image which may not have contained any information whatsoever. We remedied this by instead only looking for the lines that are indeed present in the spectrum. Overall this method finds all the line depths along every ray in every image.

The first step in this method, similarly to the previous method, is to convert the spectral image into polar coordinates. This gives the spectrum over the entire image along each of the individual rays in different azimuthal directions. Then we can use the same method to find the line depths along all those rays. In the same manner we can find the FWHM of each of these lines. We then fill in that region with contains the line and is bounded by the FWHM with the depth of that line. The output is a series of concentric rings of various sizes depending on the width of the line and then colored by the depth of the line at that point. This process is then repeated for all of the images in the data set. We can then use the same transformations used to construct the panoramic image to place the depth rings onto the scene. We found that this method gives largely the same result as the previous method.

In Figure 6.3 we can see that the two methods find a similar change in the line depth between the two regions which is seen in the histograms of the line depth. The reason for the change in the absolute value of the line depths is that in the second method we have only considered the deepest lines and ignored all of the shallower ones. In the first method all the lines are considered so the shallower lines will increase the mean fractional line depth.

This method has significant advantages over the previous method. The largest being that it does not oversample the data, in that it only extracts the data that is available and does not need to make assumptions to align the baselines of the component spectra. The other benefit, is the drastic improvement in run time. This method can finish a data set containing 20 images in just over a minute whereas the

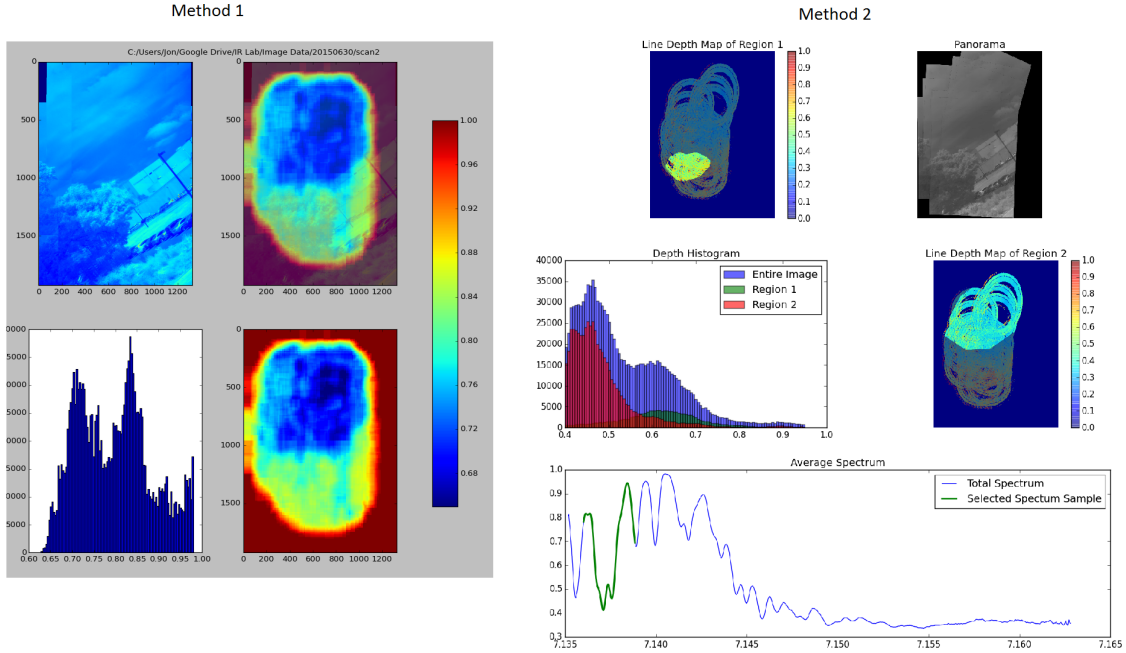


Figure 6.3: A comparison of the two different depth mapping methods on the same data set. *Left:* An example of the first method of depth mapping, Upper left: an image of the full region , Upper right: The depth map and the panoramic image of the region superimposed. Bottom right: The depth map showing the same region. Bottom left: A histogram of the line depth map, deeper lines are on the left. *Right:* An example of the line depth map created by the second method. Top left: The line depth map highlighting the region containing the tree called region 1. Top right: An image of the region. Middle right: The same depth map now highlighting the sky called region 2. Middle left: A histogram of the line depths with histograms of regions 1 and 2 shown in red and green, respectively.

previous method would have taken about 2 hours to achieve a similar result. The improvement in speed comes because the old method required about 2000 regions of different sizes, each of which required complicated image region calls which is computationally and memory intensive. The improved method requires only one function call per column and then quickly reconstructs the output using a fast image mapping function.

Chapter 7: Results

The science objective of this project is twofold, the one part is to measure the florescence of chlorophyll and the other was to measure zodiacal light. Until now we have primarily focused on the chlorophyll measurements as this is an easy application of our instrument to a diffuse object which requires high resolution spectroscopy. We also include some discussion on our first attempt at the observation of zodiacal light as well as some bright astronomical objects.

7.1 Chlorophyll Florescence

As a proof that chlorophyll fluorescence is indeed observable, we can use the methods discussed in Chapter 4 to take the average spectrum of two regions of in a panoramic image. One region with a tree (Region 1) and the other region containing only the sky (Region 2), this is shown in Figure 7.1. Looking at these two spectra simply by eye one can see that the lines are not nearly as deep in the tree as they are in the sky. We can then take the ratio of these two spectra; this should show the amount of excess produced by florescence. In this ratio we can see distinct peaks where the absorption lines occur in the solar spectrum. The height of this ratio corresponds to the fraction of the light coming from florescence [36]. In this figure

we show the results at 720 nm; here the chlorophyll florescence signal should be near its maximum [16].

Using models of chlorophyll and the solar spectrum we can make predictions about the effect of florescence on the reflectance of solar light. The total fraction of light which is observed in excess of Fraunhofer lines varies with wavelength from 0 around 600 nm to a peak of about 15% at about 740 nm. In the filters we will consider we note that the signal should be nonexistent at 590 nm, weak but observable at 656 nm, and peaked at 720 nm.

Using the tools discussed in the previous chapter we can create the line depth maps showing the mean line depth over the field of view. In the results below we have used the first method for creating the line depth maps. We then repeated this procedure using three different filters 590 nm, 656 nm, and 720 nm. The results of which are shown in Figure 7.2.

In these plots it is clear that there is a signal contained in the tree. Looking at the bottom left of the rightmost depth map (720 nm) we can see that there is a difference between the line depths on the sky and on the tree. The histogram also confirms this there are two distinct peaks in the histogram implying that the lines in the tree are shallower by about 12% (84% deep on the sky and 72% deep in the tree). This result is confirmed by the other two sets of figures. In the center set (656 nm) there is just barely a difference seen as a shoulder to the right of the main peak in the histogram at a percent difference of $\sim 5\%$. By eye, this shallower region does appear to be located on the tree compared to the sky. The final set on the left (590 nm) shows no signal in the histogram. Looking at the depth map itself there

does not appear to be any significant variation in the line depth over the panoramic image.

These results reflect the results of the simulations. We see a strong signal of florescence at 720 nm, a weak signal at 656 nm, and no signal at 590 nm. From Figure 1.4, we expected the flux at 720 nm to be about 6 times the flux at 656 nm. This is slightly stronger than the difference in line depth we observe, but there are many factors including the solar angle of incidence, which reduces the flux incident on the surface. The chlorophyll density also change this value as more chlorophyll dense plants should produce more fluorescence at constant incident radiation.

Before this project is finished we would like to make measurements in the other filters we have available. These should confirm that this effect is indeed florescence as this signal should diminish again around 800 nm, so observations with our 850 nm filter should show no signal.

7.2 Astronomical Observations

As a proof of concept we took the instrument out to the Goddard observatory and made a few observations of the sky. The primary focus of these observations was to prove the ability of this instrument to make observations of astronomical objects as well as take their spectra. We collected spectra with two FPIs in spatial scanning mode. During these observations we were able to collect spectra of the orion nebula in $H\alpha$, the moon, and Jupiter. Fainter objects will require more accurate tuning and better cameras which we should have soon. This shows that our instrument

works in practice to observe diffuse objects. The procedures and setup we have described can be used in general to take spatially resolved high resolution spectra of astronomical sources.

We also collected some data with only one FPI. This gave some spectra of bright emission sources as we did not have the contrast afforded by two FPIs to collect spectra. The primary focus was on the Orion Nebula. This object has very bright Hydrogen emission lines so could easily be seen with only one FPI, this is shown on the right hand side of Figure 7.3. In this figure we can also see a second bright line which is likely a nitrogen emission line at 654.8 or 658.4 nm both of which are within the 3.5 nm FWHM of this filter. We also observed the moon with one FPI in spatial scanning mode. We do not see the same contrast as we would with two FPIs but the $H\alpha$ absorption feature is so strong that it can still be seen while orders are overlapping [24].

The issue in analyzing this data was that the data reduction tools does not contain a star tracking routine. The panorama image creation requires there to be sharp features in an image which can be found using the SURF feature detector. This becomes a problem when working on star images because the SURF algorithm ignores point like objects and instead searches for sharp corners as features. This means that a star tracking algorithm should be used to find the stars in the field of view. We intend to implement the Astrometry.net routine to find stars in the field of view and thus determine the transformation between two images of astronomical objects [37]. We used this on a raw image of our data, shown in Figure 7.4, this shows that this was easily able to find many of the faint stars in our images. We

could then use this to find the proper transformations of our data.

7.3 Zodiacal Light

At the beginning of this project we had intended to make observations of zodiacal light by looking for the solar spectrum in a dark sky long after sunset [3]. We tested our instrument at the Goddard Space Flight Center off site observatory and discovered that our cameras are too noisy to be able to observe zodiacal light. For a one minute exposure the signal is dominated by the dark current of the hot pixels in the detector. There are on the order of 500 hot pixels, which would dominate the signal if we were to take the 10 minute exposure required to observe even a faint signal of zodiacal light from our observing site [38]. Planned upgrades to our camera will make these observations of zodiacal light possible.

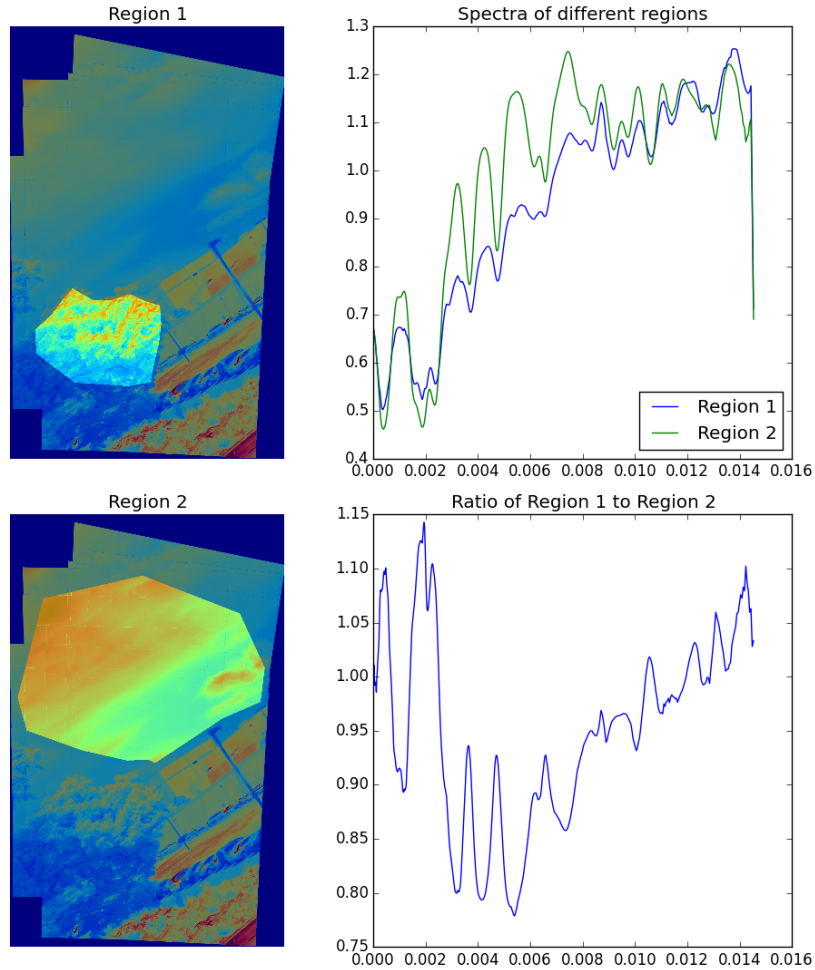


Figure 7.1: An example of the observed chlorophyll florescence signal in the 720nm filter. *Left:* The top and bottom images show the selected regions of the panorama image containing a tree with brightly lit leaves (Region 1) and the sky (Region 2), receptively. *Top right:* The average spectrum of these two regions, here the x-axis is proportional to wave-length although the absolute wavelength calibration has not been done for this dataset. *Bottom right:* The ratio of the spectrum of region 1 to the spectrum of region 2, plotted on the same scale.

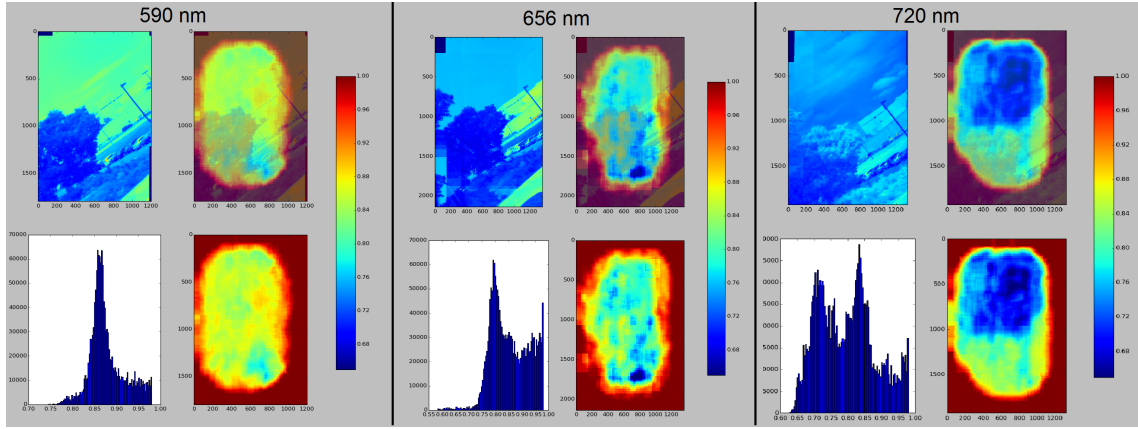


Figure 7.2: All figures show the mean line depth over the field of view. Top left: The panoramic image of the reference. Bottom right: The mean line depth map, note that the scale of the line depth map is common to all the figures and shows blue as the deepest lines and red as the shallowest. Top right: The line depth map overlaid on the panoramic image showing the relationship between the line depth and the reference. Bottom left: A histogram of the line depth map, this shows the difference in line depths at the location of the tree versus the sky. *Left:* the results at 590 nm *Center:* the results at 656 nm *Right:* the results at 720 nm.

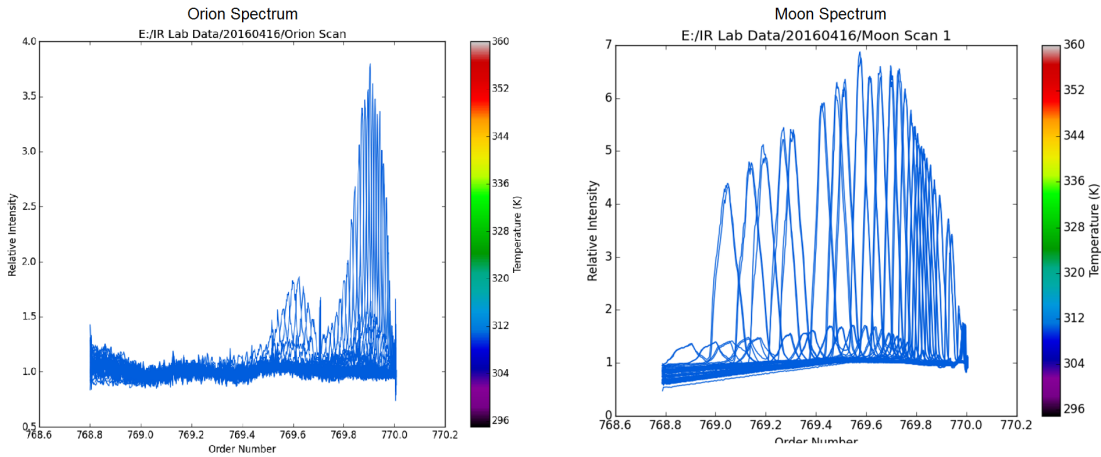
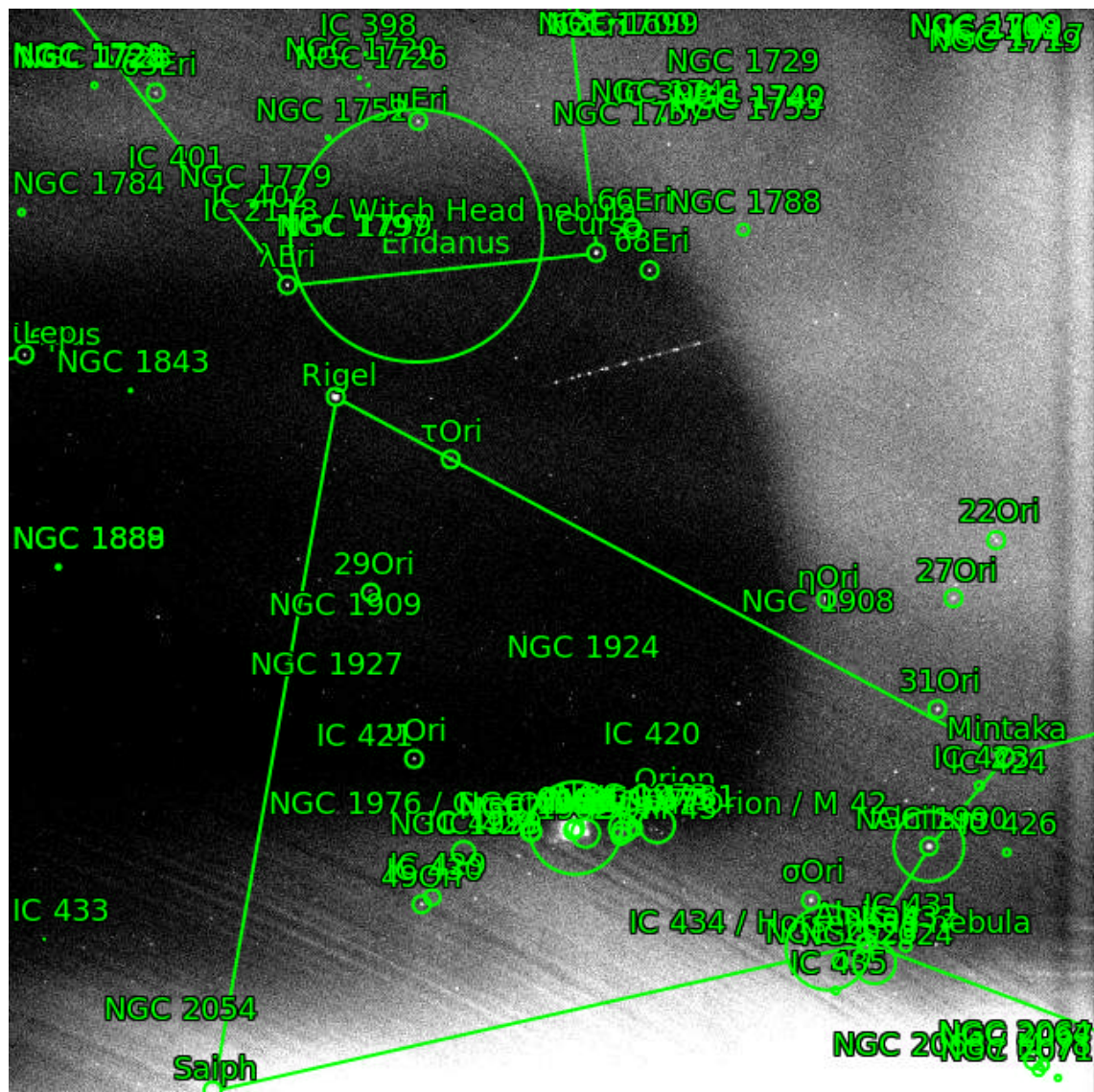


Figure 7.3: Spectra of objects collected using one FPI in spatial scanning mode. *Left:* Spectrum of Orion the peak on the right has the same order number as the lab hydrogen emission tube. *Right:* Spectrum of the moon. The second order peaks are from ghosting of the moon image.



Chapter 8: Conclusion

Through this project we have demonstrated the ability of our high resolution spectrometer to take spectra of diffuse sources. Beginning from a simple instrument with many free parameters we have developed it into a true scientific instrument. We have shown the process of designing mounts for each of the components and the testing of the assembly. A program was written to collect data, control temperatures, and perform basic analysis. We then measured the properties of the instrument focusing on the thermal properties as they are crucial to the control of the instrument.

Once the instrument was constructed we created a data reduction procedure which is robust to almost any input data. This includes all image normalization procedures like flat fielding and dark frame subtraction. It also determines all the required parameters needed for the analysis of the data including the optical center and all necessary transformations. The data reduction procedure is almost entirely automated but future improvements could simplify this process even more to require no input from the user.

Using these tools we have made measurements of the fluorescence of chlorophyll these results serve as a test of our ability to observe high resolution spectra of diffuse

objects. This involved taking high resolution spectra of a plant using the sky as a reference source. We then reconstructed the spectrum at any point in the field of view of the instrument. Using two different methods we have created maps of the line depth in a series of images. These have shown that there is a significant variation in the spectrum within a tree corresponding to the strength of the chlorophyll signal.

8.1 Future Instrument Assembly

Within the next month we should have a new assembly for the instrument. We took the issues we had with the original instrument and made modifications to fix them in a new assembly. The largest revision is that the vacuum chambers will be mounted on a fabricated tip tilt mount rather than a purchased one. A rendering of this new assembly is shown in Figure 8.1.

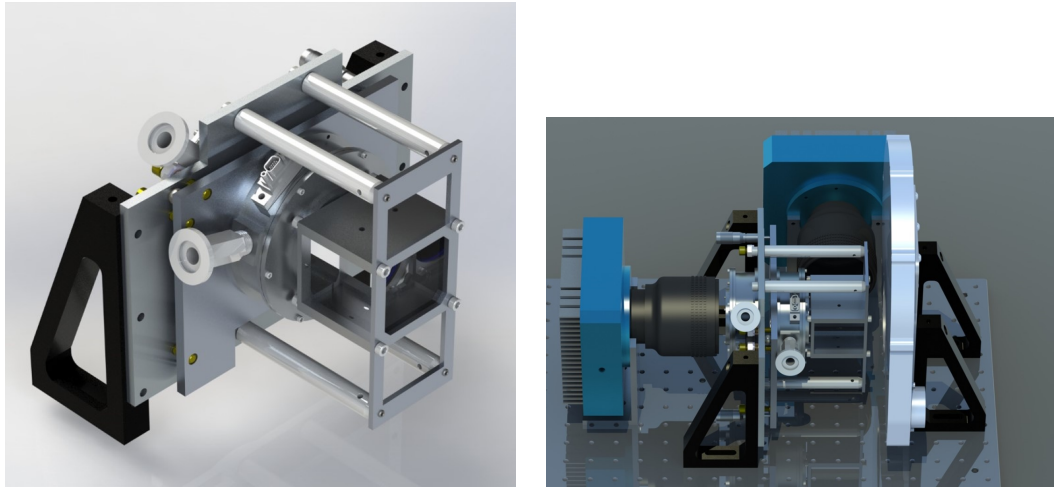


Figure 8.1: Renderings of the updated instrument. *Left:* Isometric view of the newly modeled parts including the tip tilt mount with the vacuum chamber, and beamsplitter on the right. *Right:* A rendering of the new components installed into the instrument.

Overall the scheme of observation and major components are unchanged. The mounting of the components is the only major change. In addition to the creation of the tip tilt mount we also changed the vacuum chamber to better accommodate the etalon holder. The old vacuum chamber was too tight around the holder to allow clearance for the heater and thermometer wires. In making the vacuum chamber larger it would no longer fit into the purchased tip tilt mount hence the change to our manufactured one.

When we combine this new instrument assembly with our new low noise cameras we will be able to easily to spectra of astronomical sources. The cameras will be arriving soon and will be a very significant improvement to our current cameras.

8.2 Future Observations

Within the next few months the new assembly of the instrument should be complete. This will allow us to much more easily take new measurements of both chlorophyll fluorescence and astronomical sources.

In the future, this instrument could easily be adapted to larger scale observations. There is a strong motivation to use this instrument to measure bulk plant productivity, which was observed in the chlorophyll signal. Space based or high altitude measurements of chlorophyll efficiency would be a very enticing observation for those in the biological sciences. In the field of astronomy there are many diffuse objects which would be ideal targets for this system including nebulae and bright galaxies.

Bibliography

- [1] C. van der Tol, J. A. Berry, P. K. E. Campbell, and U. Rascher. Models of fluorescence and photosynthesis for interpreting measurements of solar-induced chlorophyll fluorescence. *Journal of Geophysical Research: Biogeosciences*, 119(12):2312–2327, 2014. 2014JG002713.
- [2] T. Arai, S. Matsuura, J. Bock, A. Cooray, M. G. Kim, A. Lanz, D. H. Lee, H. M. Lee, K. Sano, J. Smidt, T. Matsumoto, T. Nakagawa, Y. Onishi, P. Korngut, M. Shirahata, K. Tsumura, and M. Zemcov. Measurements of the Mean Diffuse Galactic Light Spectrum in the 0.95-1.65 μm Band from CIBER. *ApJ*, 806:69, June 2015.
- [3] E. Grün, B.A.S. Gustafson, S. Dermott, and H. Fechtig. *Interplanetary Dust*. Astronomy and Astrophysics Library. Springer Berlin Heidelberg, 2001.
- [4] R. J. Reynolds, G. J. Madsen, and S. H. Moseley. New Measurements of the Motion of the Zodiacal Dust. *ApJ*, 612:1206–1213, September 2004.
- [5] Luca Giovannelli. Study of a fabry-pérot interferometer prototype for space applications. Master’s thesis, Università degli studi di Roma Tor Vergata, 2010.
- [6] G. Hernandez. *Fabry-Perot Interferometers*. Cambridge Studies in Modern Optics. Cambridge University Press, 1988.
- [7] Marco Q Pisani and Massimo E Zucco. *Fourier transform based hyperspectral imaging*. INTECH Open Access Publisher, 2011.
- [8] Krishnavedala. Fabry-perot diagram, mar 2013.
- [9] M. Vaughan. *The Fabry-Perot Interferometer: History, Theory, Practice and Applications*. Series in Optics and Optoelectronics. Taylor & Francis, 1989.
- [10] Klaus Betzler, Fachbereich Physik, and Universitt Osnabrück. Universitt osnabrück 1 fabry-perot interferometer fabryperot.tex kb 20020122.

- [11] R Mock, B Hillebrands, and R Sandercock. Construction and performance of a Brillouin scattering set-up using a triple-pass tandem Fabry-Perot interferometer. *Journal of Physics E: Scientific Instruments*, 20(6):656, 1987.
- [12] Jarkko Antila, Akseli Miranto, Jussi Mäkynen, Mari Laamanen, Anna Rissanen, Martti Blomberg, Heikki Saari, and Jouko Malinen. Mems and piezo actuator-based fabry-perot interferometer technologies and applications at vtt. In *SPIE Defense, Security, and Sensing*, pages 76800U–76800U. International Society for Optics and Photonics, 2010.
- [13] B. Ravindra and R. K. Banyal. A dual Fabry-Perot based narrow band imager for the National Large Solar Telescope. In *Astronomical Society of India Conference Series*, volume 2 of *Astronomical Society of India Conference Series*, 2011.
- [14] S. Veilleux, B. J. Weiner, D. S. N. Rupke, M. McDonald, C. Birk, J. Bland-Hawthorn, A. Dressler, T. Hare, D. Osip, C. Pietraszewski, and S. N. Vogel. MMTF: The Maryland-Magellan Tunable Filter. *The Astronomical Journal*, 139:145–157, January 2010.
- [15] R. J. Reynolds, S. L. Tufte, L. M. Haffner, K. Jaehnig, and J. W. Percival. The Wisconsin H α Mapper (WHAM): A Brief Review of Performance Characteristics and Early Scientific Results. *Publications of the Astronomical Society of Australia*, 15:14–18, April 1998.
- [16] C. Frankenberg, C. O’Dell, L. Guanter, and J. McDuffie. Remote sensing of near-infrared chlorophyll fluorescence from space in scattering atmospheres: implications for its retrieval and interferences with atmospheric CO₂ retrievals. *Atmospheric Measurement Techniques*, 5(8):2081–2094, 2012.
- [17] Kate Maxwell and Giles N. Johnson. Chlorophyll fluorescence: a practical guide. *Journal of Experimental Botany*, 51(345):659–668, 2000.
- [18] U. Schreiber, U. Schliwa, and W. Bilger. Continuous recording of photochemical and non-photochemical chlorophyll fluorescence quenching with a new type of modulation fluorometer. *Photosynthesis Research*, 10(1):51–62.
- [19] Christian Frankenberg, Joseph Berry, Luis Guanter, and Joanna Joiner. Remote sensing of terrestrial chlorophyll fluorescence from space. *SPIE Newsroom*, feb 2013.
- [20] Luis Guanter, Yongguang Zhang, Martin Jung, Joanna Joiner, Maximilian Voigt, Joseph A. Berry, Christian Frankenberg, Alfredo R. Huete, Pablo Zarco-Tejada, Jung-Eun Lee, M. Susan Moran, Guillermo Ponce-Campos, Christian Beer, Gustavo Camps-Valls, Nina Buchmann, Damiano Gianelle, Katja Klumpp, Alessandro Cescatti, John M. Baker, and Timothy J. Griffis. Global

- and time-resolved monitoring of crop photosynthesis with chlorophyll fluorescence. *Proceedings of the National Academy of Sciences*, 111(14):E1327–E1333, 2014.
- [21] Douglas B. Leviton, Kevin H. Miller, Manuel A. Quijada, and Tyler D. Groff. Temperature-dependent refractive index measurements of l-bbh2 glass for the subaru charis integral field spectrograph, 2015.
 - [22] K. A. Pietraszewski and A. G. Meldrum. Cryogenic servo-stabilized Fabry-Perot interferometer for imaging at 2-2.5 microns. In L. G. Burriesci and J. B. Heaney, editors, *Cryogenic Optical Systems and Instruments VII*, volume 2814 of *SPIE*, pages 139–146, October 1996.
 - [23] ICOS Optical Systems, 190-192 Ravenscroft Road, Beckenham, Kent BR3 4TW. *CS100 Controller and ET Series II Servo-stabilized Interferometer System User’s Guide*.
 - [24] F. Paletou, M. Lafon, P. Maeght, F. Grimaud, T. Louge, and J. Aboudarham. The ground-based solar observations database BASS 2000. 3 pages, 1 figure (to appear in the Procs. of Solar Polarization Workshop #5, eds. Berdyugina, Nagendra and Ramelli), December 2007.
 - [25] Tables for reference solar spectral irradiances: Direct normal and hemispherical on 37 tilted surface.
 - [26] R. Fata, V. Kradinov, and D. Fabricant. Flexure mounts for high-performance astronomical lenses. In *Society of Photo-Optical Instrumentation Engineers (SPIE) Conference Series*, volume 6269 of *SPIE*, page 62695T, June 2006.
 - [27] Brett Beauregard. Arduino pid library.
 - [28] Michael Richmond. Dark subtraction and flatfielding, apr 2002.
 - [29] J. Bland and R. B. Tully. The Hawaii imaging Fabry-Perot interferometer (HIFI). *The Astronomical Journal*, 98:723–735, August 1989.
 - [30] G. Bradski. *Dr. Dobb’s Journal of Software Tools*.
 - [31] J.E. Solem. *Programming Computer Vision with Python: Tools and algorithms for analyzing images*. Safari Books Online. O’Reilly Media, 2012.
 - [32] Matthew Brown and David G Lowe. Automatic panoramic image stitching using invariant features. *International journal of computer vision*, 74(1):59–73, 2007.
 - [33] M. Brown, R. I. Hartley, and D. Nister. Minimal solutions for panoramic stitching. In *2007 IEEE Conference on Computer Vision and Pattern Recognition*, pages 1–8, June 2007.

- [34] A. Kramida, Yu. Ralchenko, J. Reader, and NIST ASD Team. NIST Atomic Spectra Database (ver. 5.3), [Online]. Available: <http://physics.nist.gov/asd> [2016, April 24]. National Institute of Standards and Technology, Gaithersburg, MD., 2015.
- [35] Reardon, K. P. and Cavallini, F. Characterization of fabry-perot interferometers and multi-etalon transmission profiles. *A&A*, 481(3):897–912, 2008.
- [36] J. Joiner, L. Guanter, R. Lindstrot, M. Voigt, A. P. Vasilkov, E. M. Middleton, K. F. Huemmrich, Y. Yoshida, and C. Frankenberg. Global monitoring of terrestrial chlorophyll fluorescence from moderate spectral resolution near-infrared satellite measurements: methodology, simulations, and application to GOME-2. *Atmospheric Measurement Techniques Discussions*, 6:3883–3930, April 2013.
- [37] D. Lang, D. W. Hogg, K. Mierle, M. Blanton, and S. Roweis. Astrometry.net: Blind Astrometric Calibration of Arbitrary Astronomical Images. *The Astronomical Journal*, 139:1782–1800, May 2010.
- [38] A. C. Levasseur-Regourd and R. Dumont. Absolute photometry of zodiacal light. *Astronomy and Astrophysics*, 84:277–279, April 1980.